A Cable-Driven Soft Robotic Hand With an In-Hand RGB-D Camera for Dexterous Grasping and Manipulation

Zhanfeng Zhou, *Member, IEEE*, Runze Zuo, *Student Member, IEEE*, Matthew Du, Shaojia Wang, Sebastian Levy, *Member, IEEE*, Yu Sun, *Fellow, IEEE*, and Xinyu Liu, *Member, IEEE*

***Abstract*—The aspiration to replicate the capabilities of the human hand has driven innovations in the design of soft robotic hands. Despite these advancements, many existing designs of soft hands still lack effective in-hand vision and the ability for each finger to achieve active multidegree-of-freedom motion. This article proposes a cable-driven soft robotic hand that can achieve dexterous grasping and manipulation, vision-guided grasping, vision-based slip detection and compensation, as well as visually servoed in-hand manipulation. The hand has five soft fingers, each capable of independent flexion/extension motion and bidirectional ad/abduction motion. A red–green–blue-depth (RGB-D) camera is integrated into the palm of the soft hand to enable in-hand vision capability. Modeling of the soft hand is established to analyze its kinematics, statics, and manipulability. A series of experiments are conducted to demonstrate its dexterous grasping and manipulation capabilities on a variety of objects. Using 3-D point cloud data from the in-palm camera, an effective vision-guided grasping strategy is developed to grasp objects on a table. The in-hand vision also enables slip detection and compensation during grasping to maintain the grasp stability. Furthermore, a hierarchical, visually servoed controller is developed to perform closed-loop in-hand object manipulation. With its high dexterity and visual feedback capabilities, the soft hand will find important applications such as household object manipulation and food picking/sorting, and may also be used as a prosthetic hand or an auxiliary hand for humans.**

***Index Terms*—Cable-driven soft hand, dexterous grasping, in-hand manipulation, in-hand vision, vision-based control.**

Received 30 June 2025; accepted 6 October 2025. Date of publication 9 December 2025; date of current version 16 January 2026. This work was supported in part by the Natural Sciences and Engineering Research Council of Canada under Grant RGPIN-2022-05039, in part by the Canada Foundation for Innovation under Grant JELF-38428, in part by the University of Toronto CARTE Seed Fund University of Toronto Percy Edward Hart Professorship. This article was recommended for publication by Associate Editor J. Zhao and Editor H. Zhao upon evaluation of the reviewers' comments. *(Corresponding authors: Yu Sun; Xinyu Liu.)*

Zhanfeng Zhou, Matthew Du, Shaojia Wang, Yu Sun, and Xinyu Liu are with the Department of Mechanical and Industrial Engineering, University of Toronto, Toronto, ON M5S 3G8, Canada (e-mail: zhanfeng.zhou@mail.utoronto.ca; matthew.du@mail.utoronto.ca; shawnjia.wang@mail.utoronto.ca; sun@mie.utoronto.ca; xyliu@mie.utoronto.ca).

Runze Zuo is with the Department of Mechanical Engineering, University of Michigan, Ann Arbor, MI 48104 USA (e-mail: zuorunze@umich.edu).

Sebastian Levy is with the Department of Mechanical Engineering, Carnegie Mellon University, Pittsburgh, PA 15213 USA (e-mail: sebastianlevy@cmu.edu).

This article has supplementary downloadable material available at https://doi.org/10.1109/TRO.2025.3641751, provided by the authors.

Digital Object Identifier 10.1109/TRO.2025.3641751

I. Introduction

THE human hand is of vital importance to human life due to its advanced dexterity to handle objects of various shapes, sizes, and materials. Developing a robotic hand to mimic the dexterous grasping and manipulation functions of a human hand has been an essential challenge in robotics [1], [2].

Various human-like robotic hands have been designed recently [3], [4], [5], [6]. The dominant form is the rigid robotic hand, which is generally acknowledged for its high load-carrying capacity, fast motion speed, and high operation accuracy [7], [8], [9], [10], [11], [12]. In contrast, the soft robotic hand, which is intrinsically flexible and compliant, possesses some unique advantages, including a lightweight structure, excellent morphological adaptability to unknown object shapes, and high safety levels during human interactions [13], [14], [15], [16]. Thus, soft robotic hands are particularly suitable for grasping and manipulating unknown or fragile objects and for tasks requiring safe robot–human interactions [17], [18], [19], [20].

There are mainly two types of soft robotic hands based on their actuation methods: fluid-driven (pneumatic or hydraulic) [21], [22], [23] and cable-driven soft robotic hands [24], [25], [26], [27], [28], [29], [30], [31], [32], [33], [34], [35], [36], [37], [38], [39]. Compared to pneumatic soft hands, cable-driven soft hands enable more rapid control and larger actuation forces for finger movements, thus meeting higher grasping and manipulation requirements. Also, they can offer enhanced durability without concerns about rupture failures or fluid leakage, which are common issues for pneumatic soft hands.

Many researchers have contributed to the development of cable-driven soft robotic hands. Most of these hands feature a basic finger design that can only perform flexion/extension (F/E) motion [24], [25], [26]. While some designs incorporate both adduction/abduction (AD/AB) and F/E motions in the thumb, the remaining fingers are still restricted to F/E motions [27], [28], [29], [30], [31], [32]. This contrasts with the human hand, where each finger can perform both F/E and AD/AB movements. As a result, these designs can only achieve basic grasping and manipulation capabilities. The absence of active AD/AB joints in the fingers significantly limits their dexterity for complex grasping and manipulation tasks.

In recent developments, some cable-driven soft robotic hands with fingers capable of performing both F/E and AD/AB motions

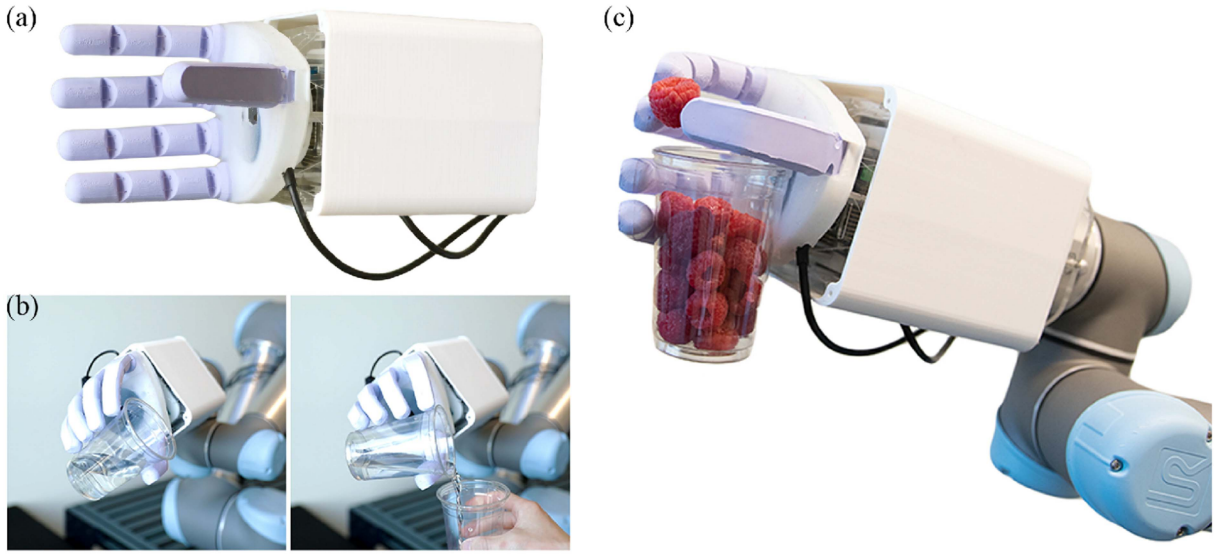

Fig. 1. Cable-driven soft robotic hand. (a) Photograph of the soft hand. (b) Soft hand collaborates with the human hand and pours water using only finger movement. (c) Soft hand simultaneously grasps a fragile raspberry and a plastic cup filled with raspberries.

have been developed. Kontoudis et al. [33], [34] designed a cable-driven soft hand consisting of five monolithic soft fingers, each featuring flexure F/E joints and a spring-loaded AD/AB joint. Similarly, Yan et al. [35], [36] developed a soft hand with five 3-D-printed cable-driven nylon fingers. The middle finger is actuated by a single motor for F/E motion and the other fingers are each actuated by two motors for both F/E and AD/AB motions. However, in these hands, the AD/AB motion of the fingers (except the thumb) is restricted to a unilateral direction, spreading away from the middle finger, which enhances grasping capabilities but contributes little to in-hand manipulation. For instance, these hands are unable to realize 6-degree-of-freedom (6-DOF) in-hand manipulations, as discussed in Section IV-B, which involves translation and rotation along the x-, y-, and z-axes [9], [21]. The iRobot-Harvard-Yale (iHY) soft hand [37], [38] and other Yale OpenHand designs [39], [40], [41], [42] employ rotary joints at the finger base, enabling finger rotation along a fixed axis. However, these joints cannot replicate the lateral AD/AB movements of human hands; instead, their functions are to transition the hands between different grasp configurations [37], [38], [39], [40] or rotate objects for in-hand regrasping during gaited manipulation [41], [42]. To date, the dexterous in-hand manipulation capability of human-like cable-driven soft robotic hands, where each soft finger independently performs F/E and bidirectional lateral AD/AB motions, has not been fully studied.

Integrating visual feedback into robotic hands can significantly enrich their sensing modalities and improve their grasping and manipulation capabilities. Two common camera configurations are eye-to-hand and eye-in-hand [43], [44]. Eye-to-hand setups provide a comprehensive view of both the hand and objects but typically require external cameras and additional space for setup [45], [46], [47], [48]. In contrast, eye-in-hand cameras are more portable and can provide a more direct and dynamic perspective of objects from various views by moving with the hand [49], [50]. Yet, for a human-like soft robotic hand, a compact in-hand vision system that fully integrates an RGB-D camera into the palm, providing visual feedback during both grasping and in-hand manipulation stages, has not been demonstrated to date.

To address the aforementioned limitations, this article proposes a cable-driven soft robotic hand with integrated in-hand vision for dexterous grasping and manipulation, vision-guided grasping, vision-based slip detection and compensation, as well as visually servoed in-hand manipulation. Our hand has five soft fingers, each actuated by two motors through cables and capable of independently performing F/E motion and bidirectional AD/AB motion. Mathematical models are established for the soft hand to analyze its kinematics, statics, and manipulability, and characterization is performed to analyze finger and hand performance. The dexterous grasping and manipulation capabilities of the soft hand are demonstrated through a series of experiments. Moreover, an RGB-D camera is integrated into the palm of the soft hand to enable in-hand vision capability. Based on the 3-D point cloud data captured by the in-palm camera, the position and orientation of unknown objects on a table can be determined, and an effective vision-guided strategy is generated to grasp the objects. The in-hand vision also enables slip detection and compensation during grasping to maintain grasp stability. Additionally, a hierarchical visually servoed controller is developed to perform closed-loop in-hand object manipulation. Given its prominent dexterity and manipulation capabilities, the soft hand is suitable for diverse applications, such as fruit picking and sorting, household object grasping and manipulation, and serving as a prosthetic or extra hand for humans.

II. Design, Materials, and Methods

A. Overall Design

The soft robotic hand is designed with several unique features. *1) Human-like design:* The structure and configuration

TABLE I
PARAMETERS OF THE SOFT HAND

Parameters (units)	Value
Dimensions of the soft hand (length × width × height) (mm)	114 × 114 × 135
Dimensions of the entire system with motor base (length × width × height) (mm)	118 × 118 × 280
Net weight of the soft hand (g)	385
Total weight of the entire system with motors (g)	1200
Dimensions of soft fingers (except thumb) (mm) $(l_a + l_b + l_c + l_d + l_e)$	$31 + 29 + 31 + 15$ $+15$
Dimensions of the thumb (mm) $(l_b + l_c + l_d + l_e)$	$32 + 33 + 18$ $+18$

of the soft hand are inspired by the human hand to replicate its essential features and functions. The soft fingers mimic the musculoskeletal structure with an endoskeleton embedded inside and actuated tendons routed along the finger body and the endoskeleton. *2) High dexterity:* Each finger is capable of independently performing F/E motion and bidirectional AD/AB motion, enabling high dexterity for human-like grasping and manipulation. *3) Integrated in-hand vision system:* An RGB-D camera is embedded in the palm of the soft hand, enabling vision-based grasping and manipulation. Compared to the commonly used wrist-mounted configurations, the in-palm camera offers a consistent unobstructed view of the object throughout the grasping and manipulation process. These unique features empower the soft hand to perform a wide range of dexterous tasks, as detailed in Section IV.

When the human hands grasp and manipulate objects in daily life, the most common and effective configuration of the fingers is that the thumb is opposed to the other four fingers. In this configuration, human hands can perform both pinch grasp and power grasp, as well as complicated manipulation tasks. To replicate the essential functions of human hands, the soft hand was designed based on a human-like configuration, where four identical soft fingers are vertically arranged along one side of the palm, and a soft thumb is positioned at a 60° angle to the palm and opposite to the other fingers, as shown in Fig. 2(a). The dimensions and weight of the hand are listed in Table I. The soft finger consists of a monolithic soft finger body made of silicone materials and a flexible 3-D-printed endoskeleton integrated inside the finger body [see Fig. 2(d)].

Each finger is actuated by two motors through a cable-driven system and can perform both F/E and bidirectional AD/AB movements independently. Therefore, the dexterous soft hand has 10 DOFs for five fingers and is actuated by ten motors (Dynamixel AX-12A, ROBOTIS Inc.) through a motor controller (Arbotix-M Robocontroller, Trossen Robotics), which can be arranged compactly within the hand base. The motor is selected due to its compact size and sufficient stall torque (1.5 N·m at 12 V), which fulfills the actuation requirements of the soft fingers. Each motor is assembled with a customized 3-D-printed spool connected to the driving cable [see Fig. 2(c)], where the rotary motion of the motor is converted to the linear motion of the

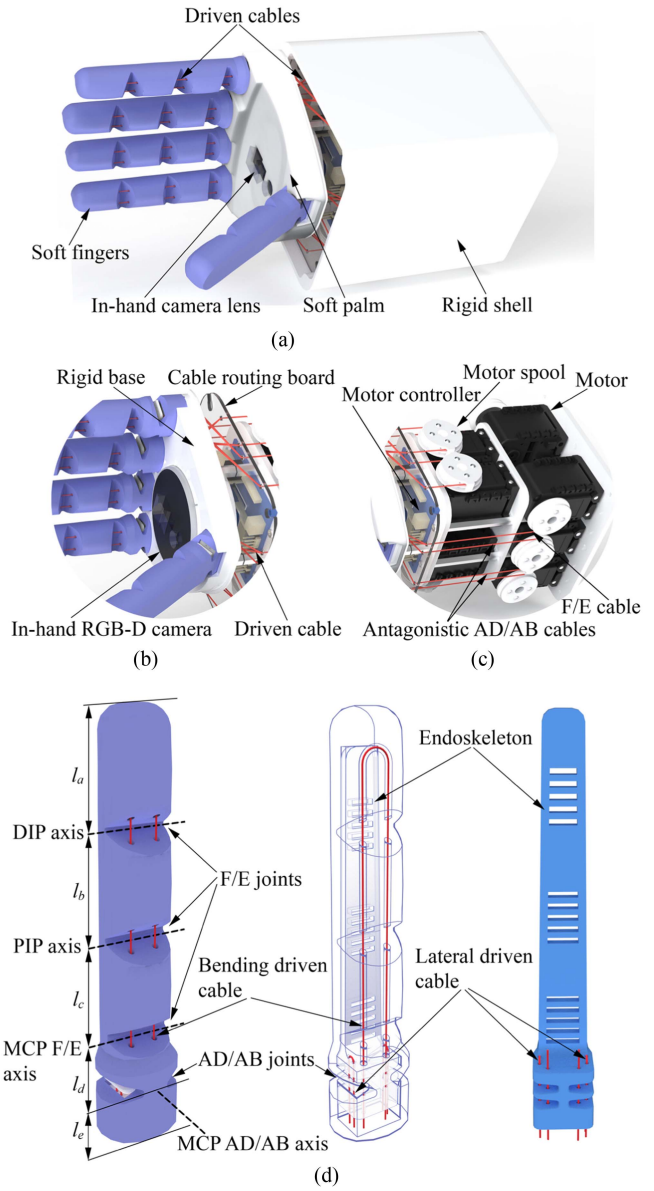

Fig. 2. Overall design of the soft hand. (a) Soft hand with a soft silicone palm and a 3-D-printed rigid shell. (b) Hand base with an in-palm camera. (c) Cable-driven system of the soft hand. (d) Structure of the soft finger with an endoskeleton inside.

cable. Additionally, a compact RGB-D camera (L515, Intel RealSense) is embedded within the palm [see Fig. 2(b)], which ensures that the objects are not blocked by the robotic arm and hand during grasping and manipulation. The camera also supports object detection, vision-guided grasping, and visually servoed in-hand manipulation, which will be introduced in Sections IV-C and IV-E.

B. Design of the Soft Fingers

The human finger is composed of rigid bones and joints covered with soft tissues and skin, and is actuated by muscle groups located on the forearm. Between the bones and muscles, the tendon group routed through the hand serves as the transmission

system that can deliver forces and torques to the finger joints for F/E and AD/AB movements. Most existing soft robotic hands have a finger design with either a pure-elastomer finger body or rigid phalanges connected by elastic joints [24], [25], [26], [27], [28], [29], [30], [33], [34], both of which lack sufficient lateral stiffness to resist unexpected lateral forces. Inspired by the musculoskeletal structure of the human finger, our soft finger consists of a monolithic finger body that is fully compliant, an endoskeleton embedded inside the finger body, and a cable transmission mechanism that connects the soft fingers to the motors in the hand base [see Fig. 2(d)]. The integrated endoskeleton not only provides the AD/AB joint for the lateral movement of the soft finger but also enhances its lateral stiffness, allowing the finger to resist unexpected lateral forces. Moreover, due to strategically placed patterns on the endoskeleton at F/E joint areas, the joint stiffness is increased to enhance force output and payload capacity of the finger and thus enable more robust grasping and manipulation.

The soft finger body is molded by soft silicone materials (Smooth-Sil 945), and the flexible endoskeleton is 3-D-printed with flexible polyurethane (TPU 95A). The soft finger has three F/E soft joints and one AD/AB soft joint [see Fig. 2(d)], which is designed to mimic the movement of the 1-DOF proximal interphalangeal (PIP) and distal interphalangeal (DIP) joints, and the 2-DOF metacarpophalangeal (MCP) joints of the human finger. The soft joints are defined by notches on the finger body, aligned with cutoffs on the endoskeleton. Our soft finger body has a notch angle of 60° for the three identical F/E soft joints and 30° for the AD/AB soft joints. The notch angles on the finger body also determine the range of bending angle and AD/AB angle of the soft finger. The dimensions of the finger phalanges (l_a, l_b, and l_c) were selected based on anthropometric data of the human finger [51], while also considering functional requirements of grasping and manipulation. Similar lengths among the three phalanges help distribute contact more evenly and ensure that the distal phalanx can achieve sufficient surface contact and pressure during power grasp. Additionally, two base extensions (l_d and l_e) were incorporated to accommodate the MCP joint's AD/AB mechanism and to provide supports and connections between the fingers and the palm. The soft thumb is an exception with only two F/E soft joints and one AD/AB soft joint; thus, l_a is not included in the thumb's parameters. The parameters for the four identical soft fingers and the thumb are all listed in Table I.

C. Cable Actuation System

The cable actuation system is crucial to enabling the F/E and bidirectional AD/AB motions of the soft robotic fingers. For F/E motion, a single cable (nylon cable, 0.3 mm in diameter) is routed through the soft finger body [see Fig. 2(d)] and attached to a motor spool on the other side following the route through the hand base [see Fig. 2(c)]. When the motor spool pulls the cable, the finger will bend at the F/E soft joints, and elastic energy will be stored in the soft joints to restore the soft finger to its original straight shape if the cable is released. To enable bidirectional AD/AB motion, two additional cables are routed through both sides of the endoskeleton at the AD/AB joints [see Fig. 2(d)].

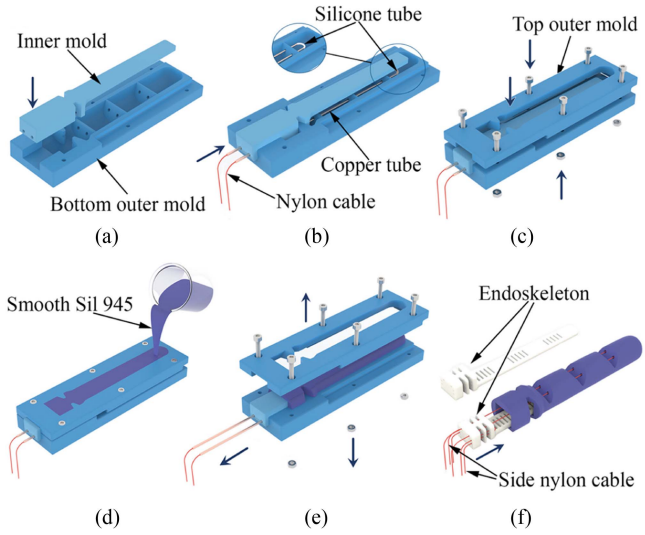

Fig. 3. Fabrication process of the cable-driven soft finger. (a) Prepare 3-D-printed molds of the finger body and assemble the inner mold onto the bottom outer mold. (b) Insert two metal tubes through the assembled mold with a soft silicone tube connecting them, and a single nylon cable is routed through both metal and silicone tubes. (c) Assemble the top mold and screw the nuts and bolts to secure all molds together. (d) Cast uncured Smooth-Sil 945 material into the assembled mold; the finger body forms after a 6-hour curing period. (e) Pull out the two metal tubes, unscrew the nuts and bolts, and remove the top mold and inner mold, leaving the nylon cable routed along the finger body and the silicone tube inside the fingertip. (f) 3-D-print an endoskeleton for the soft finger based on soft material (TPU 95A), then insert the endoskeleton into the finger body and route three nylon cables through it.

These two cables are connected to a single motor spool in an antagonistic fashion [see Fig. 2(c)]. When the motor rotates in one direction, the motor spool will pull the cable on one side of the AD/AB joints and release the cable on the other side so that the soft finger can move laterally. This antagonistic mechanism not only supports bidirectional AD/AB motion but also balances the lateral actuation forces of the soft fingers.

D. Fabrication of the Soft Fingers

One significant challenge in fabricating the soft finger is that the routing path of the cable and the hollow structure of the endoskeleton must be fabricated during the molding process of the soft finger body before integrating the 3-D-printed compliant endoskeleton. To address this, we developed a fabrication method based on hybrid deposition manufacturing (HDM) [52], as illustrated in Fig. 3. First, a pair of rigid outer molds, which define the external geometry of the soft finger body, along with a rigid inner mold shaped to the contours of the endoskeleton, are 3-D-printed. Then, the inner mold is assembled into the lower outer mold [see Fig. 3(a)], and two steel tubes are inserted through the assembled mold. A nylon cable (diameter: 0.3 mm) for bending movement is threaded through the steel tubes and a soft silicone tube. After that, the soft silicone tube is configured in a U-shape to connect the two steel tubes at their ends [see Fig. 3(b)]. This integration ensures that the cable is pre-routed within the finger body during the molding process, thereby eliminating the challenging task of threading the cable through

the U-shaped path in the fingertip after the finger body is formed. Next, the top mold is secured to the existing assembly using nuts and bolts [see Fig. 3(c)], after which a silicone release agent (Ease Release 200 from Smooth-On, Inc.) is sprayed on the inner surfaces of the assembled mold. Subsequently, uncured silicone material (Smooth-Sil 945 with 45 Shore-A hardness from Smooth-On, Inc.) is cast into the assembled mold, and the soft finger body forms after a 6-hour curing period [see Fig. 3(d)]. When the material is cured, the two steel tubes are first removed, resulting in two routing paths for the cable. The finger body is then demolded with the U-shape silicone tube and the soft nylon cable left within it, as shown in Fig. 3(e). The endoskeleton of the finger is 3-D-printed using flexible polyurethane (Ultimaker TPU 95A with 95 Shore-A hardness from Ultimaker B.V.), with rectangular cutoffs at the position of the soft flexion joints and notches cutting on each side at the position of the soft ad/abduction joints [see Fig. 3(f)]. The bending body of the endoskeleton is designed to gradually narrow from bottom to top at a 2° angle, facilitating easy integration within the finger body. Finally, the cable for finger bending is inserted through the endoskeleton, and two new nylon cables are routed through both sides of the endoskeleton for finger lateral movement, after which the endoskeleton is integrated inside the finger body with silicone rubber adhesive (Sil-Poxy from Smooth-on, Inc.) [see Fig. 3(f)].

III. Modeling and Characterization

In this section, the kinematic and static models of the soft fingers are first established. Then, we characterize the soft fingers and the soft hand experimentally. Finally, the manipulability of the soft hand is modeled to understand its dexterous manipulation capability within its workspace.

A. Modeling of the Soft Fingers

Since the soft finger is lightweight and its F/E and AD/AB movements are relatively slow, only the kinematic and static models were derived in this section, which will be used to control the soft hand in the following grasp and manipulation experiments (Sections IV-A and IV-B).

The deformation of the soft finger occurs mainly in its soft joints during actuation. In the conventional pseudo-rigid link model [53], the soft finger is usually represented as rigid links connected by ideal rigid revolute joints, as illustrated in Fig. 4(a). Finger F/E and AD/AB movements based on the pseudo-rigid link model are illustrated in Fig. 4(b) and (d), respectively. However, the behavior of soft joints differs from that of rigid revolute joints with a fixed rotation center. The rotation center of soft joints can shift dynamically during deformation. To better capture this behavior, the rotation centers in the model were offset to more closely match the actual motion of soft joints, resulting in an adjusted pseudo-rigid link model, as shown in Fig. 4(c) and (e). The adjusted model demonstrates improved accuracy in kinematics modeling, as validated by experiments in Section III-B. For each finger—pinky (P), ring finger (R), middle finger (M), index finger (I), and thumb (T)—the following notation is used: ABD represents the rigid AD/AB joint,

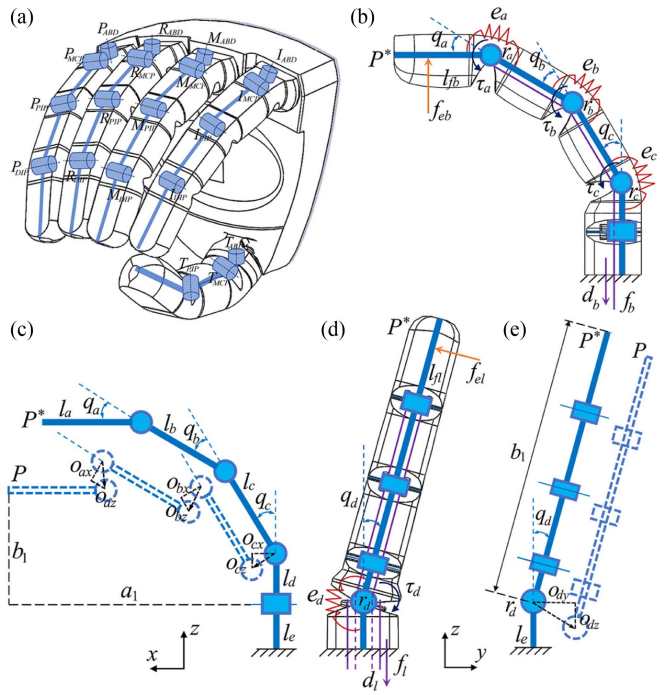

Fig. 4. Modeling of the soft hand and the cable-driven soft finger. (a) Joint notations and pseudo-rigid links of the soft hand. (b) Pseudo-rigid link model of a soft finger performing F/E movement. (c) Adjusted pseudo-rigid link model for finger F/E movement. (d) Pseudo-rigid link model of a soft finger performing AD/AB movement. (e) Adjusted pseudo-rigid link model of finger AD/AB movement.

and MCP, PIP, and DIP denote the three F/E joints. For example, P_{ABD} represents the rigid AD/AB joints of the pinky. In this section, only the modeling of soft fingers, except for the thumb, is discussed, since the thumb can be modeled using the same methods.

First, the kinematic model is developed based on the adjusted pseudo-rigid link model. As shown in Fig. 4(c), during finger F/E movement, rotation centers of the three corresponding rigid F/E joints are offset by $O_a = [o_{ax} \quad o_{az}]^T$, $O_b = [o_{bx} \quad o_{bz}]^T$, and $O_c = [o_{cx} \quad o_{cz}]^T$, respectively. For AD/AB movement, the rotation center of the AD/AB joint is offset by $O_d = [o_{dy} \quad o_{dz}]^T$, as shown in Fig. 4(e). These offset vectors are defined in the local coordinate system of each joint, and their components depend on the corresponding joint angles. The expressions for these offsets are derived in the subsequent modeling process. $P = [x \quad y \quad z]^T$ denotes the fingertip position, while P^* is the fingertip position derived from the original pseudo-rigid link model. Finger joint angles are represented by $Q = [q_a \quad q_b \quad q_c \quad q_d]^T$. Two cables actuate the rigid finger joints, one cable (displacement: d_b) is to actuate the F/E joints (q_a, q_b, q_c), and the other cable (displacement: d_l) is to actuate the AD/AB joints (q_d). The cable displacements are defined as $D = \begin{bmatrix} d_b & d_l \end{bmatrix}^T$.

The position of the fingertip P can be expressed as

$$x = a_1 \tag{1a}$$

$$y = o_{dy} + b_1 s_d \tag{1b}$$

$$z = l_e + o_{dz} + b_1 c_d \tag{1c}$$

where

$$\begin{bmatrix} a_1 \\ b_1 \end{bmatrix} = \begin{bmatrix} o_{cx} \\ l_d + o_{cz} \end{bmatrix} + \begin{bmatrix} c_c & s_c \\ -s_c & c_c \end{bmatrix} \begin{bmatrix} o_{bx} \\ l_c + o_{bz} \end{bmatrix} + \begin{bmatrix} c_{bc} & s_{bc} \\ -s_{bc} & c_{bc} \end{bmatrix} \begin{bmatrix} o_{ax} \\ l_b + o_{az} \end{bmatrix} + \begin{bmatrix} c_{abc} & s_{abc} \\ -s_{abc} & c_{abc} \end{bmatrix} \begin{bmatrix} 0 \\ l_a \end{bmatrix} \tag{2}$$

and we assume that $s_{abc} = sin(q_a + q_b + q_c)$, $s_{bc} = sin(q_b + q_c)$, $s_c = sin(q_c)$, $c_{abc} = cos(q_a + q_b + q_c)$, $c_{bc} = cos(q_b + q_c)$, $c_c = cos(q_c)$.

Given that the three F/E soft joints have the same structures and dimensions, we adopted the same functional form for their offset vectors and assumed equal F/E joint angles ($q = q_a = q_b = q_c$). Specifically, the offset components for each joint were modeled as a second-order polynomial function of the corresponding joint angle

$$\begin{bmatrix} o_{ax} \\ o_{az} \end{bmatrix} = \begin{bmatrix} o_{bx} \\ o_{bz} \end{bmatrix} = \begin{bmatrix} o_{cx} \\ o_{cz} \end{bmatrix} = \begin{bmatrix} \alpha_x q + \beta_x q^2 \\ \alpha_z q + \beta_z q^2 \end{bmatrix} \tag{3}$$

$$\begin{bmatrix} o_{dy} \\ o_{dz} \end{bmatrix} = \begin{bmatrix} \gamma_y q_d + \delta_y {q_d}^2 \\ \gamma_z q_d + \delta_z {q_d}^2 \end{bmatrix} \tag{4}$$

where α_x, β_x, α_z, β_z are offset coefficients for the F/E joint, and γ_y, δ_y, γ_z, δ_z are the offset coefficients for the AD/AB joint. While the second-order formulation is a simplification, it provides a balance between model complexity and fitting accuracy, as demonstrated in the characterization experiments in Section III-B.

Then, by differentiating (1), the relationship between the fingertip position P and the soft joint angles Q can be expressed as

$$\Delta P = J_P \Delta Q \tag{5}$$

where J_P is the Jacobian matrix which maps from the joint angle space to the fingertip position in the Euclidean space.

Next, the relationship between the actuated cable displacements D and the soft joint angles Q can be expressed as

$$\Delta D = J_r \Delta Q \tag{6}$$

where J_r is the transmission distribution Jacobian matrix that relates the joint angle space to cable displacement space

$$J_r = \begin{bmatrix} r_a & r_b & r_c & 0 \\ 0 & 0 & 0 & r_d \end{bmatrix} \tag{7}$$

where r_a, r_b, r_c, and r_d are the radii of revolute joints, as shown in Fig. 4(b). The radii of the three F/E revolute joints are assumed to be equal: $r = r_a = r_b = r_c$ due to identical dimensions of the three soft F/E joints.

The two driving cables are connected to the spools of two motors, with r_{mb} and r_{ml} representing the radii of the spools for finger bending and lateral motions, respectively. Then, the relationship between the actuated cable displacements $D = \begin{bmatrix} d_b & d_l \end{bmatrix}^T$ and the motor angles $Q_m = \begin{bmatrix} q_{mb} & q_{ml} \end{bmatrix}^T$ takes the form of

$$\Delta D = J_m \Delta Q_m \tag{8}$$

$$J_m = \begin{bmatrix} r_{mb} & 0 \\ 0 & r_{ml} \end{bmatrix} \tag{9}$$

where J_m is the transmission distribution Jacobian matrix that maps the motor angle space to the cable displacement space.

Combining and solving (6) and (8) yield

$$J_r \Delta Q = J_m \Delta Q_m \tag{10}$$

which represents the relationship between the finger joint angles and the motor angles.

Consequently, the relationship between the fingertip position P of the soft finger and the motor angles Q_m can be established by combining (5) and (10), which takes the form of

$$\Delta P = J_p J_r^+ J_m \Delta Q_m \tag{11}$$

where $J_r^+ = J_r^T (J_r J_r^T)^{-1}$ is the Moore-Penrose inverse (pseudoinverse) matrix of J_r.

Due to the highly nonlinear nature of the forward kinematic equations of the soft finger, a closed-form inverse kinematic solution is not feasible. Instead, the widely used Jacobian-based inverse kinematics is employed to control the soft finger. When we have a desired fingertip position, the required joint angles can be obtained through

$$\Delta Q = J_P^+ \Delta P \tag{12}$$

where $J_p^+ = J_p^T (J_p J_p^T)^{-1}$ is the Moore-Penrose inverse matrix of J_p, and motor angles are updated by

$$\Delta Q_m = {J_m}^{-1} J_r J_P^+ \Delta P. \tag{13}$$

Actuation of the motor can ensure accurate control of the fingertip position during the grasping and manipulation experiments, as presented in Sections IV-A and IV-B.

After the kinematic analysis, a static balance analysis of the soft finger is performed. The static equilibrium equations take the form of

$$J_e^T F_e = \mathcal{T} - E \Delta Q \tag{14}$$

$$\mathcal{T} = J_r^T F_t \tag{15}$$

where $\mathcal{T} = \begin{bmatrix} \tau_a & \tau_b & \tau_c & \tau_d \end{bmatrix}^T$ is the internal joint torque vector, and $F_t = \begin{bmatrix} f_b & f_l \end{bmatrix}^T$ is the cable tension force vector, as shown in Fig. 4(b). E is the elastic matrix of the soft finger, given by

$$E = \begin{bmatrix} e_a & 0 & 0 & 0 \\ 0 & e_b & 0 & 0 \\ 0 & 0 & e_c & 0 \\ 0 & 0 & 0 & e_d \end{bmatrix} \tag{16}$$

where e_a, e_b, e_c, and e_d are the elastic coefficients of each soft finger joint, respectively [see Fig. 4(b)]. $F_e = \begin{bmatrix} f_{eb} & f_{el} \end{bmatrix}^T$ is the external force applied on the soft finger. For statics analysis

TABLE II
OFFSET COEFFICIENTS OF THE ADJUSTED PSEUDO-RIGID LINK MODEL

	F/E joint				AD/AB joint			
	α_x	β_x	α_z	β_z	γ_y	δ_y	γ_z	δ_z
Fingers	0.38	2.78	−2.79	−3.16	−1.83	−3.72	−1.48	3.60
Thumb	0.21	1.78	−2.24	−2.88	−1.76	−2.55	−2.56	3.14

of the soft finger, researchers usually focus on the case where the external force is normally applied on the distal phalanx of the finger, corresponding to the pinch grasp of a soft hand [38], [53], [54]. We also perform the static analysis of the pinch-grasp case here, as shown in Fig. 4(b). J_e^T is the Jacobian matrix for the external forces, given by

$$J_e^T = \begin{bmatrix} l_{fb} & 0 \\ c1 & 0 \\ c1 + (l_c - o_{bz})c_{ab} & 0 \\ 0 & b1 - (l_a - l_{fl})c_{abc} \end{bmatrix} \tag{17}$$

where $c1 = l_{fb} + (l_b - o_{az})c_a$, $c_a = cos(q_a)$, $c_{ab} = cos(q_a + q_b)$, l_{fb} is the distance between the bending external force f_{eb} and the DIP joint, and l_{fl} is the distance between the lateral external force f_{el} and the DIP joint.

The two motors actuating the cables provide torques $\mathcal{T}_m = \begin{bmatrix} \tau_{mb} & \tau_{ml} \end{bmatrix}^T$ to the spools, and the spools will wind the cables and provide pulling forces to drive the fingers. Based on the kineto-static duality, the relation between the motor torques $\mathcal{T}_m$ and the cable tension forces F_t is given by

$$\mathcal{T}_m = J_m^T F_t. \tag{18}$$

Finally, substituting (15) and (18) into (14) yields

$$J_e^T F_e = J_r^T (J_m^T)^{-1} \mathcal{T}_m - E\Delta Q \tag{19}$$

which represents the required motor torques $\mathcal{T}_m$ to actuate the soft fingers at specific joint angles Q and external forces F_e.

For any fingertip positions and desired fingertip output forces of the soft fingers, the required motor torque can be computed by combining two constraint equations (5) and (19).

B. Characterization of the Soft Fingers

After theoretically modeling the soft hand, we conducted experiments to characterize finger performance. Only the characterization of the four identical soft fingers is discussed in this section, and the thumb was characterized using the same method.

First, to evaluate the forward kinematics of the adjusted pseudo-rigid link model (1), fingertip trajectories of the soft finger were captured during both F/E and AD/AB movements, as shown in Fig. 5. The experimental trajectories were used to identify the joint offset coefficients in (3) and (4) by fitting them to the trajectories predicted by the adjusted model through the least-squares regression method. The results of the offset coefficients for both F/E and AD/AB joints are summarized in Table II. We then compared the predicted fingertip trajectories generated by the adjusted model with the experimentally measured data.

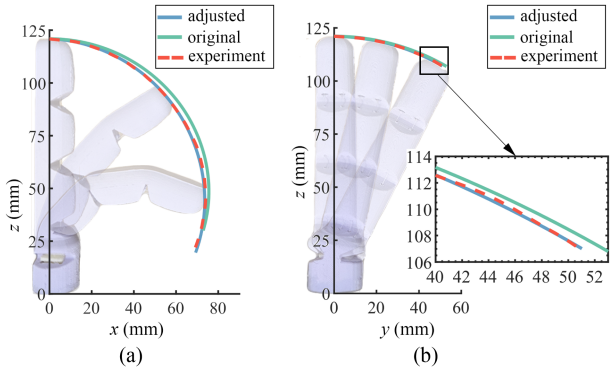

Fig. 5. Comparison of fingertip trajectories between the experimental data, the adjusted pseudo-rigid link model, and the original pseudo-rigid link model. (a) Fingertip trajectories during finger F/E movement as the fingertip bending angle increases from 0° to 145°. (b) Fingertip trajectories during finger AD/AB movement as the fingertip AD/AB angle increases from 0° to 30°.

Fig. 5(a) and (b) presents detailed comparisons of the experimental fingertip trajectories with those predicted by the adjusted and original pseudo-rigid link model, during finger F/E and AD/AB movement, respectively. For F/E movement (fingertip bending angle: 0°–145°), the root-mean-square error (RMSE) between the adjusted model prediction and experimental trajectory was 0.86 mm, which is significantly lower than the 6.23 mm RMSE obtained using the original model. For AD/AB movement (fingertip AD/AB angle: 0°–30°), the adjusted model prediction achieves an RMSE of 0.45 mm with respect to the experimental trajectory, compared to an RMSE of 1.09 mm with the original model. These experimental results demonstrate that the adjusted model, which incorporates joint-angle-dependent offset terms to joint center positions, can significantly reduce the fingertip trajectory deviation compared to the original model and more accurately reflect the actual kinematics of the soft finger. This improved accuracy validates that the proposed adjusted model is capable of capturing the complex deformation and nonlinear behavior of the soft joints in the soft finger.

Next, the relationships between cable actuation and the resulting fingertip motions are characterized. Fig. 6(a) and (b) illustrates the experimental setups, including a finger holder, a moving slider, a force sensor connecting the cable of the soft finger and the moving slider, a rotary motor with an encoder, and a lead screw to convert motor rotary motion to linear motion. The soft finger was attached to the finger holder and the cable was pulled by the moving slider at a constant speed. During the experiments, the fingertip remained unloaded to isolate and characterize the intrinsic bending or AD/AB behavior of the finger, and thus the external force was considered to be zero. When the soft finger moved, the cable displacement was calculated from the rotary encoder (sampling frequency: 10 Hz), and the cable tension force was measured simultaneously by the force sensor (sampling frequency: 10 Hz).

First, the relationships between cable displacements and the resulting fingertip bending and AD/AB angles were determined. The fingertip angles at specific cable displacements were measured from the image frames [see Fig. 6(a) and (b)] and fitted to

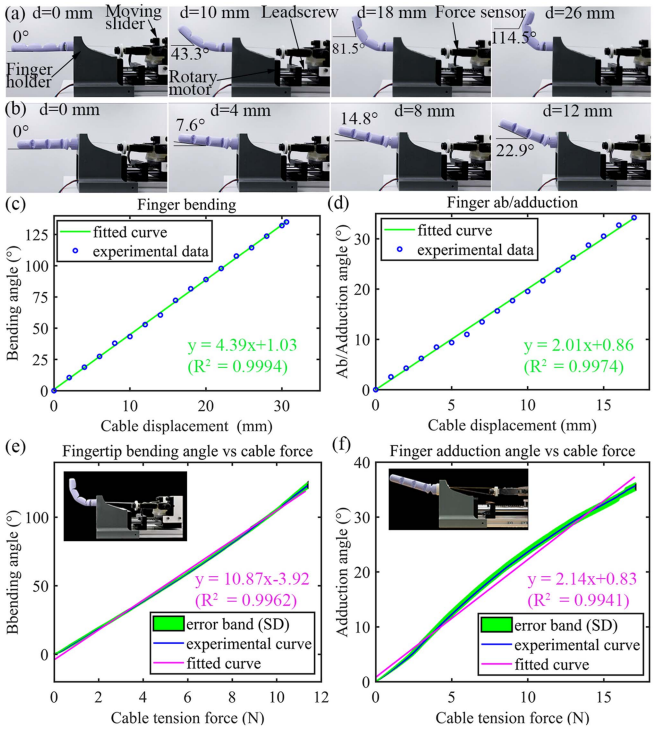

Fig. 6. Experimental characterization of the soft fingers. (a) Photographs of the finger bending motion at different cable displacements. (b) Photographs of the finger adduction motion at different cable displacements. (c) Experimental data and fitted characterization curve for the fingertip bending angle as a function of cable displacement. (d) Experimental data and fitted characterization curve for the adduction angle as a function of cable displacement. (e) Experimental curve (n = 5) and fitted characterization curve for the fingertip bending angle versus the cable tension force. (f) Experimental curve (n = 5) and fitted characterization curve for the fingertip adduction angle versus the cable tension force. The green error band represents the standard deviation across five tests.

linear curves as functions of cable displacements [see Fig. 6(c) and (d)]. Both angles increase linearly with cable displacements, and this is consistent with our theoretical kinematic modeling (6) in Section III-A. The fitted linear relationships were then employed to calculate the parameters of the soft finger kinematic model (6), including the radii of the flexion revolute joints (r_a, r_b, r_c) and the ad/abduction revolute joints (r_d). Results are shown in Table III. With the experimentally characterized kinematic model, the fingertip position and the finger configuration can be controlled precisely through the adjustment of the motor angles during the grasping and manipulation experiments in Sections IV-A and IV-B.

Subsequently, the relationships between the cable tension force and the corresponding fingertip bending and AD/AB angles were established. After the cable displacements and cable tension force were collected during finger movements, the cable displacements were converted into fingertip bending and ad/abduction angles based on the linear relationships presented in Fig. 6(c) and (d). This procedure was repeated five times, and the resulting curves are illustrated in Fig. 6(e) and (f). Based on the linear theoretical static balance model (14) of the soft finger, linear curves were used to fit the experimental curves with minimum error [see Fig. 6(e) and (f)]. These fitted linear curves

TABLE III
PARAMETERS OF SOFT FINGER THEORETICAL MODEL

Parameters (units)	Value
The radius of F/E revolute joints of soft fingers (except thumb, $r_a = r_b = r_c$) (mm)	4.35
The radius of F/E revolute joints of the thumb (mm)	4.64
The radius of AD/AB revolute joints of soft fingers (except thumb, r_d) (mm)	28.5
The radius of AD/AB revolute joints of the thumb (mm)	27.9
The radius of the motor spool ($r_{mb} = r_{ml}$) (mm)	12
The elastic coefficient of F/E revolute joints of soft fingers (except thumb, $e_a = e_b = e_c$) (mm·N)	22.9
The elastic coefficient of AD/AB revolute joints of soft fingers (except thumb, e_d) (mm·N)	762.1
The elastic coefficient of F/E revolute joints of the thumb (mm·N)	43.6
The elastic coefficient of AD/AB revolute joints of the thumb (mm·N)	831.2

were then used to calculate the parameters (e_a, e_b, e_c, e_d) in the static balance model (14). Results are shown in Table III. Potential sources of error between the characterized linear curves and experimental curves include the rigid-link assumption and possible cable extension during finger movement.

C. Characterization of the Soft Hand

The grasping capacity of the soft hand is analyzed in this subsection, including the dimensional limits of objects that can be grasped and the maximum payload. A typical cylinder object was selected to characterize the soft hand, because the soft fingers can easily conform to the surface of the cylinder and fully envelop it during a power grasp, and can also make stable contact with the cylinder surface during a pinch grasp [22].

A geometric analysis of the soft hand was first performed based on its Solidworks 3-D model to determine the diameter limits of the cylinder objects that can be stably grasped. Fig. 7(a)–(c) shows the results for two different grasp modes: the pinch grasp and the power grasp. When the soft hand grasps objects in the power grasp mode (the object is enveloped firmly by all the fingers), the minimum diameter of the cylinder object that can be grasped stably is 25 mm [see Fig. 7(b)]. When the soft hand grasps objects in the pinch grasp mode (only the fingertips of all the fingers are used to grasp the objects), the minimum diameter of the cylinder object that can be grasped stably is 15 mm [see Fig. 7(c)]. For both the pinch grasp mode and the power grasp mode, the maximum diameter of the cylinder object that can be grasped is 92 mm [see Fig. 7(a)].

Fig. 7(d) and (e) depicts the experimental setups for measuring the maximum horizontal and vertical payload of the soft hand, respectively. A force gauge (FG-3005 Digital Force Gauge, Shimpo) was connected via cables to the cylinder grasped by the soft hand. During measurement, the force gauge incrementally pulled the cylinder along the vertical direction until it began to slip from the grasp. The maximum payloads for the vertical and

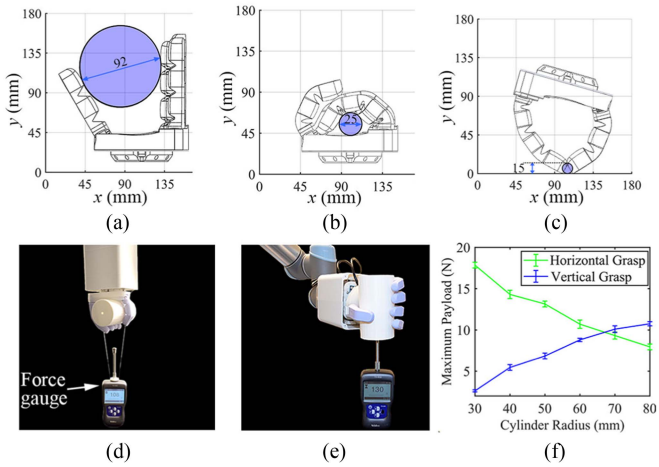

Fig. 7. Characterization of the soft hand. (a) Maximum diameter of the cylinder objects grasped stably in both pinch and power grasp modes. (b) Minimum diameter of the cylinder objects grasped stably in power grasp mode. (c) Minimum diameter of the cylinder objects grasped stably in pinch grasp mode. (d) Experimental setup for measuring the maximum horizontal payload. (e) Experimental setup for measuring the maximum vertical payload. (f) Maximum horizontal and vertical payload at different cylinder diameters.

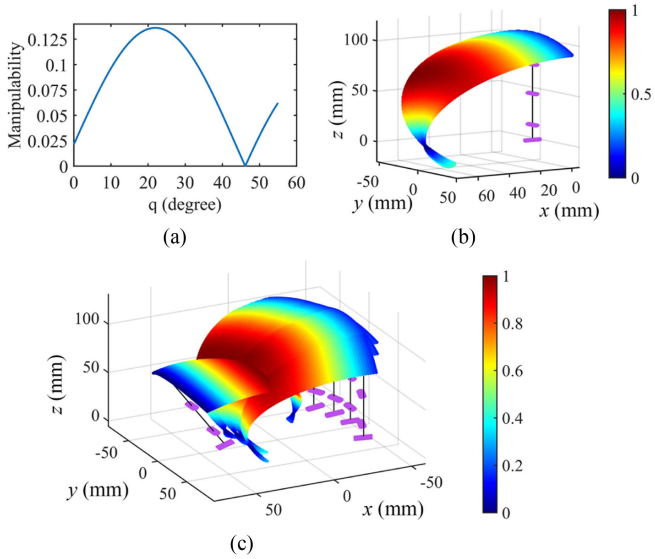

Fig. 8. Manipulability and workspace analysis. (a) Manipulability measure of the soft finger versus the joint angles of three bending joints. (b) Workspace and distribution of manipulability of a soft finger. (c) Workspace and distribution of manipulability of the soft hand.

horizontal grasps were recorded at the point of slippage. Initially, a cylinder with a diameter of 60 mm served as the test object. The maximum horizontal payload was measured to be 16.2 N [see Fig. 7(d)], while the maximum vertical payload was 8.5 N (approximately half of the maximum payload of the horizontal grasp) [see Fig. 7(e)].

Since the maximum payloads vary with different object sizes, a series of cylinders of different dimensions (radius) was then 3-D-printed and tested. The results are displayed in Fig. 7(f). As object dimensions decrease, the soft hand can fully envelop the object, thereby increasing the maximum horizontal payload. Conversely, as object dimensions increase and the soft hand cannot completely envelop the object, the horizontal payload decreases. For vertical payload, reducing object dimensions leads to a decrease in the force exerted by each soft finger, thus lowering the maximum payload. However, increasing object dimensions enhances the finger force applied to the cylinder surface, consequently raising the maximum vertical payload.

D. Manipulability Measure of the Soft Hand

In this section, the manipulability of the soft hand and its soft fingers are analyzed to evaluate their manipulation capability (see Fig. 8). For in-hand manipulation, the pinch grasp, involving only fingertips during object grasping, allows for more dexterous and precise manipulation. Thus, we only focus on the pinch grasp for the manipulability measure of the soft hand, which is a common practice in previous studies [55], [56], [57]. Additionally, we assume that soft fingers remain in unloaded conditions throughout the analysis since the objects manipulated in our experiments (Sections IV-B and IV-E) are light enough to be neglected.

The quantitative manipulability measure, proposed by Yoshikawa [58], is an effective tool to evaluate the degree of dexterity of robotic manipulators in the 3-D space

$$w = \sqrt{\det(J_P(Q)J_P(Q)^T)} \tag{20}$$

where $J_P(Q)$ denotes the Jacobian matrix of the soft finger at posture Q and maps from the joint angle space to the fingertip position in the Euclidean space, as derived in (5). Since the Jacobian matrix $J_P(Q)$ is a function of joint posture $Q = [q_a \quad q_b \quad q_c \quad q_d]$, the manipulability measure w can be computed for any given joint configuration under unloaded conditions.

First, we plot the manipulability measure w of the soft finger versus its bending joint angle q at the initial ad/abduction joint angle ($q_d = 0°$), as shown in Fig. 8(a). The bending joint angle of 21.9° produces the maximum manipulability of the soft finger with a value of 0.136. Next, to visualize the manipulability distribution in 3-D space, we compute the unloaded workspace of the soft hand by determining the fingertip positions of all soft fingers across a range of joint postures at 0.5° intervals. The normalized manipulability value $w_{\text{norm}} = \text{norm}(w)$ is then calculated at each fingertip position. A color map is employed to depict the manipulability distribution throughout the 3-D workspace of the soft finger, as shown in Fig. 8(b). The high manipulability region ($w_{\text{norm}} \geq 0.5$) appears at the bending joint angle from 5.9° to 37.9° and the ad/abduction joint angle from −30° to 30°. Fig. 8(c) depicts the manipulability distribution of the soft hand by combining the manipulability distribution of all soft fingers. The high manipulability region ($w_{\text{norm}} \geq 0.5$) appears at the central part of the workspace. During in-hand manipulation tasks, it is crucial to strategically utilize this high manipulability region to optimize the manipulation performance of the soft hand, as it provides optimal conditions for the soft

Fig. 9. Proposed soft hand is capable of realizing all 33 grasp postures of the GRASP taxonomy [59].

hand to manipulate objects with increased dexterity and efficiency. Therefore, in the following in-hand manipulation experiments presented in Sections IV-B and IV-E, objects were grasped to align within this high manipulability region throughout the manipulation process to leverage the maximum manipulation capability of the soft hand. This approach not only facilitates smoother manipulation processes but also contributes to a higher success rate in manipulation tasks.

IV. Experiments and Results

After completing the modeling and characterization of the soft hand, a series of grasping and manipulation experiments were conducted to assess its performance. Initially, the dexterous grasping and manipulation capabilities of the soft hand were demonstrated. Subsequently, vision-guided grasping, vision-based slip detection and compensation, and visually servoed in-hand manipulation experiments were performed based on the in-hand RGB-D camera.

A. Grasping Experiments

To evaluate the grasping capabilities of the proposed soft hand, we conducted a series of experiments based on the GRASP taxonomy [59], which is a widely recognized and comprehensive classification of human grasp types that includes 33 distinct postures. For each grasp type, the actuation cables of the hand were manually adjusted to replicate the corresponding finger configuration. A set of representative objects with varying shape, size, and weight was selected to match the taxonomy. A grasp was considered successful if the hand could maintain a stable hold on the object for at least 10 s without slippage. As illustrated in Fig. 9, the soft hand successfully performed all 33 grasp postures of the GRASP taxonomy. This performance is enabled by the human-like design of the hand, which enables independent F/E and AD/AB motions in each finger, closely replicating the biomechanical behavior of the human hand.

Next, the dynamic grasping capability was tested. The soft hand was mounted on a UR5 robotic arm to pick up various objects from a table. A new object set was determined based on items from the YCB Object set [60] and additional daily-use objects. An open-loop control method based on the kinematic model in Section III-A was employed. For each object, the required fingertip positions P_h and the corresponding motor input Q_i were empirically determined based on the object dimensions. Demonstrations of the hand grasping and lifting all the objects are provided in Fig. 10 and the supplemental Movie S1 and S2. Both top-down grasp and side grasp were tested successfully. When grasping small or flat objects on a table, a tilt angle of 17.5°

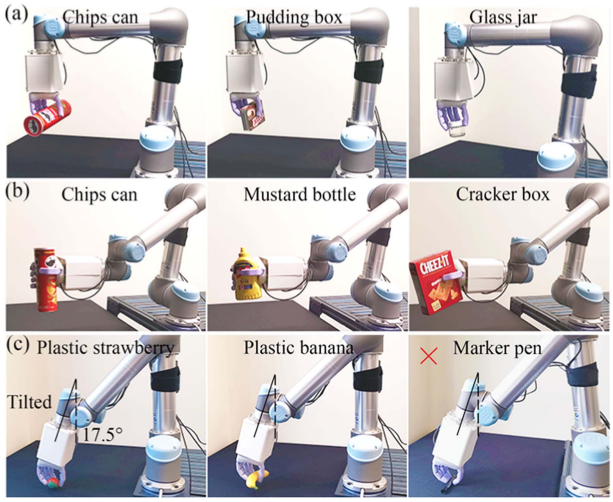

Fig. 10. Grasping and lifting objects from a table. (a) Top–down grasp. (b) Side grasp. (c) Grasping small and flat objects. The red cross mark indicates that the grasping experiment failed.

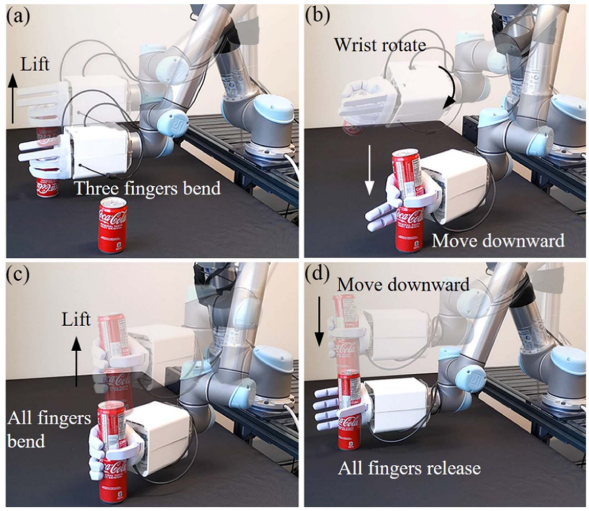

Fig. 11. Dexterous grasping experiments for picking up two Coke cans. (a) Soft hand grasps the first can by bending three fingers (thumb, index finger, and middle finger). (b) Hand rotates by 180° and approaches the second can from above. (c) Other two fingers (ring finger and little finger) bend to grasp the second can, supported by the soft palm. (d) Hand lifts both Coke cans simultaneously.

was introduced [see Fig. 10(c)] to keep fingertips of all fingers at the same level and prevent early contact with the table before grasping. The hand successfully lifted the plastic strawberry and banana but failed to grasp the screwdriver, scissors, and marker pen because their diameters are less than the minimum grasping limit (presented in Section III-C). These failures illustrate the current limitation of the finger design in grasping small or flat objects from a flat surface. Future work will aim to address this by integrating adaptive fingertips or introducing mechanical refinements to the soft fingers to enhance the versatility of the hand.

Furthermore, the soft hand demonstrated the ability to grasp delicate objects and simultaneously grasp multiple objects. Due to its soft and compliant finger structure, the hand can grasp delicate and fragile objects safely and stably. For example, it successfully lifted a glass bottle full of wine and placed it in a new location (see Supplemental Movie S1). It can also grasp a raw egg without causing breakage (see the supplemental Movie S3). Simultaneous grasping of multiple objects was realized by independent F/E and AD/AB movements of each soft finger. Fig. 1(c) shows the soft hand grasping a delicate raspberry with the thumb, index finger, and middle finger, while the other two fingers were abducted and flexed to hold a bottle full of raspberries. The coordinated use of both F/E and AD/AB motions allowed the fingers to adjust their lateral spacing, enabling independent grasping of two distinct objects. Another experiment was also conducted in which the hand grasped two Coke cans placed at different locations on the table, as shown in Fig. 11 and the supplemental Movie S3. First, it grasped the first can using three fingers (thumb, index finger, and middle finger) [see Fig. 11(a)]. Then it lifted and rotated the can by 180° before approaching the second can from above [see Fig. 11(b)]. Next, the ring and little fingers were abducted to increase inter-finger spacing, and then bent to grasp the second can, supported by the soft palm [see Fig. 11(c)]. Finally, the hand lifted both cans simultaneously and relocated them to a new location [see Fig. 11(d)]. A similar experiment demonstrating the grasp of two plastic oranges was also conducted and presented in the supplemental Movie S3. These experiments showcase the delicate and dexterous grasping capability of the soft hand.

B. Dexterous Manipulation

Dexterous in-hand manipulation is a crucial capability of human hands, realized by the multi-DOF movements of individual fingers. The proposed soft hand aims to mimic this functionality through independently F/E and bidirectional lateral AD/AB motions of each soft finger. To evaluate its manipulation performance, a series of experiments were conducted, including continuous object rotation, transferring a rod between fingers, pouring water from a cup, manipulating two pokers, single-handed cap opening, and a 6-DOF in-hand object manipulation test. Similar to experiments in Section IV-A, open-loop control was employed in these experiments. As discussed in Section III-D, maintaining the object within the high manipulability region ($w_{\text{norm}} \geq 0.5$) of the soft hand is crucial for fully leveraging its dexterity and enhancing the success rate of manipulation tasks. In the subsequent manipulation experiments, objects were selected and grasped to align within the high manipulability region [see Fig. 8(c)] of the soft hand.

First, a continuous object rotation task was demonstrated using a heuristically designed finger gait. The finger gait involves a four-step cycle that enables continuous rotation of objects. A case study was conducted to unscrew the lid of a jar on a table, as depicted in Fig. 12 and the supplemental Movie S4. Initially, a glass jar was stabilized on the table at a fixed location, while the UR5 robotic arm moved the soft hand to approach the glass jar from above, with all soft fingers remaining released in their initial pose, as shown in Fig. 12(a). Subsequently, the thumb and the other four fingers moved laterally in opposite directions—the thumb moving to the lateral left and the other four fingers to the

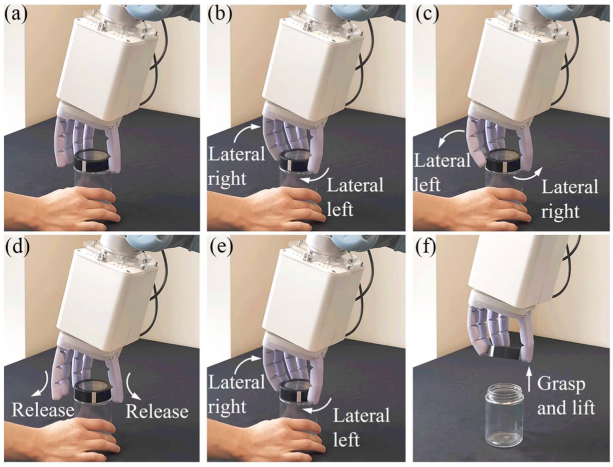

Fig. 12. Unscrewing the lid of a jar. (a) Initial pose. (b) Thumb and the other four fingers move laterally in the opposite direction to the predefined starting point and grasp the lid. (c) Then, all fingers move laterally in reverse directions to rotate the lid. (d) Release the lid. (e) All fingers return to the starting point and grasp the lid again. (f) After repeating the above unscrewing finger gait several times, the hand lifts the lid of the jar.

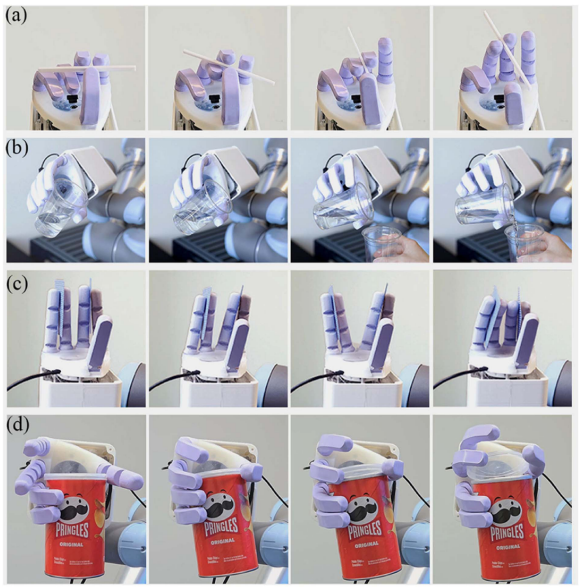

Fig. 13. Dexterous manipulation experiments. (a) Transferring a rod between fingers. (b) Pouring water from a cup. (b) In-hand manipulation for two pokers. (d) Opening the cap of a container using a single hand.

lateral right—to a predefined start point, and then bent to grasp the jar lid firmly, as shown in Fig. 12(b). Next, all fingers moved in reverse directions to rotate the lid [see Fig. 12(c)]. After this, all fingers released the lid [see Fig. 12(d)] and returned to the starting point and bent to grasp the lid again [see Fig. 12(e)]. Finally, after three repetitions of the unscrewing finger gait, the jar lid was unscrewed and lifted, as shown in Fig. 12(f). Using such a heuristic finger gait, the soft hand can rotate objects of varying shapes and sizes and operate like a human hand. A similar experiment to unscrew the cap of a bottle was also conducted and demonstrated in the supplemental Movie S4.

Next, four representative in-hand manipulation tasks were conducted, as illustrated in Fig. 13 and the supplemental Movie S4 and S5. In the between-fingers rod transfer task shown in Fig. 13(a), a rod was initially pinched between the thumb, index, and middle fingers. Then it was rotated through coordinated AD/AB movements of these three fingers and shifted to a re-grasp between the middle and ring fingers, with the ring finger adducted toward the middle finger for a secure grasp. Another task involved tilting a water-filled cup held at the fingertips to pour water into a second cup. Gradual rotation of the cup was achieved by lateral AD/AB movements of the thumb and fingers in opposite directions, as shown in Fig. 13(b). In the poker manipulation task, two pokers were grasped by the index–middle finger pair and the ring-little finger pair separately. Their independent AD/AB movements were used to simultaneously manipulate both pokers, as shown in Fig. 13(c). Finally, the soft hand performed a single-handed cap opening task, as shown in Fig. 13(d). The ring finger and pinky stabilized a container against the palm while the thumb and middle finger grasped and separated the lid using lateral AD/AB motion directed away from the stabilizing fingers. These tasks demonstrate the essential role of bidirectional AD/AB motion in dexterous in-hand manipulation.

In the final experiment, a 6-DOF in-hand object manipulation test was conducted to evaluate dexterous manipulation capabilities based on the manipulation taxonomy benchmark [59]. The test object, typically an empty Coke can, was manipulated to realize six types of in-hand motions, including translations and rotations along the x-, y-, and z-axes, similarly to experiments in [9] and [21]. During the experiment, the soft hand initially grasped the test object in pinch grasp mode without slippage, which is considered as the starting point for the test (the origin of the measurements). Then, predefined finger motions were executed to perform the six in-hand manipulations of the test object. All six tasks were successfully achieved, as shown in Fig. 14(a)–(f). For translational movements, the x-axis motion (-20.8 to 14.9 mm) was achieved by the lateral motion of all soft fingers in the same direction [see Fig. 14(a)]. The y-axis translation (-11.5 to 22.5 mm) was generated by the thumb and the opposing four fingers bending/releasing in opposite directions [see Fig. 14(b)]. The z-axis translation (-9.1 to 4.8 mm) was comparatively smaller, which requires all soft fingers to bend and release simultaneously [see Fig. 14(c)]. This coordinated movement ensures a parallel trajectory along the z-axis, allowing the object to be translated stably without slipping. For the rotational movements, the x-axis rotation (-27.8° to 20.1°) and the z-axis rotation (-17.6 to 21.9°) showed comparable results, while the y-axis rotation (-15.4° to 13.7°) had a smaller range [see Fig. 14(d)–(f)]. The x-axis rotation employed the same finger motions as the y-axis translation, indicating that these movements are coupled during in-hand manipulation. Rotation about the y-axis involves AD/AB of the thumb and coordinated bending of other fingers, while the z-axis rotation requires opposite AD/AB movements of the thumb and its opposing fingers.

C. Vision-Guided Grasping

After demonstrating the dexterous grasping and manipulation of the soft hand, vision-guided grasping was demonstrated

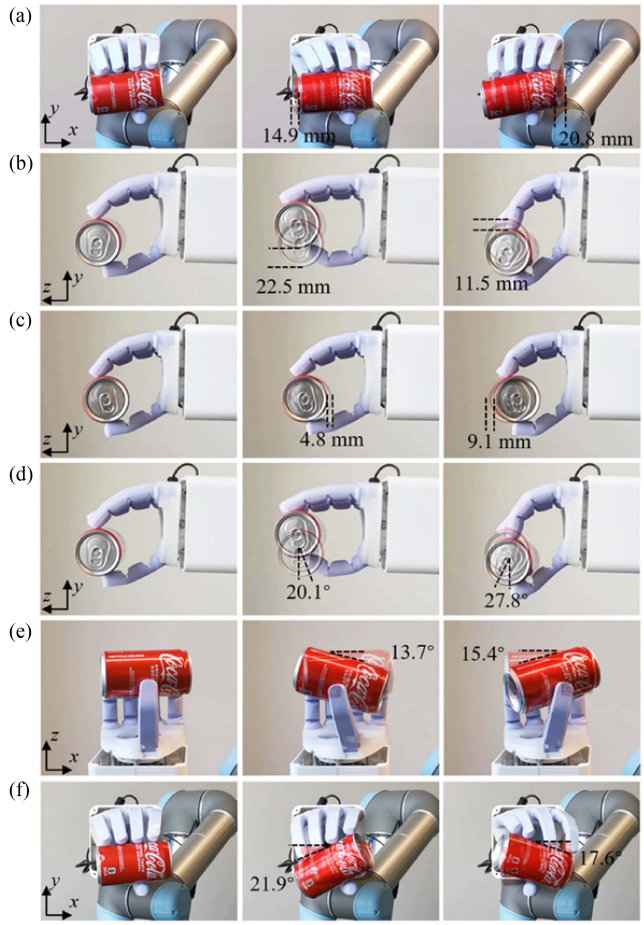

Fig. 14. 6-DOF in-hand object manipulation test. (a) Translation along the *x*-axis. (b) Translation along the *y*-axis. (c) Translation along the *z*-axis. (d) Rotation along the *x*-axis. (e) Rotation along the *y*-axis. (f) Rotation along the *z*-axis. The object grasped in the initial grasping stage, shown in the first column, was considered the starting point and the origin for the test.

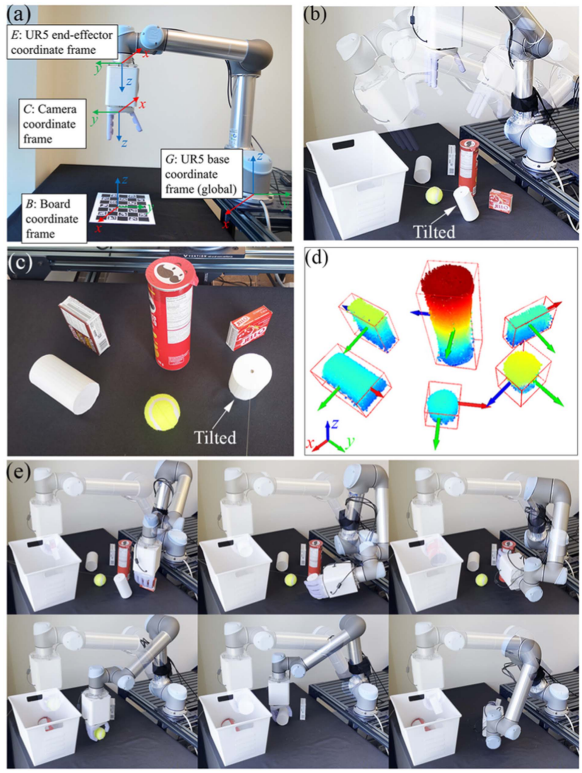

Fig. 15. Vision-guided grasping experiment of the soft hand with an in-hand RGB-D camera. (a) Online hand-eye calibration of the in-hand camera with definitions of the coordinate frames for the entire system. (b) Object scanning using the in-hand RGB-D camera of the soft hand. (c) Six objects of different sizes, shapes, and poses were placed on the table for vision-guided grasping experiments. (d) Processed point cloud image of all the objects with MVBB generated for each object. The axes of the soft hand coordinate frame show the grasp orientation derived based on the MVBB. (e) Steps to grasp each object from one side of the table to the other with the derived grasp pose and collect the object in a box.

by using the in-hand vision. Minimum volume bounding box (MVBB) algorithm [61], [62], which approximates the object point cloud with several boxes, has been widely utilized to determine the pose of unknown objects. In this experiment, to focus on the vision-guided grasping capability of the entire soft hand system, the MVBB method was adopted for the unknown objects placed on a table in unknown poses, as illustrated in the supplemental Movie S6. Additionally, our in-hand vision could allow learning-based methods for grasp planning and manipulation in more complex real-world scenarios [63], [64], [65], [66], which will be explored in our future work.

At the beginning of vision-guided grasping, the online hand–eye calibration of the in-hand camera was first performed to find its relative position and orientation with respect to the UR5 end-effector coordinate frame (*E*) (hand–eye transformation matrix H_C^E). Definitions of the coordinate frames for the entire system are shown in Fig. 15(a).

During the online hand–eye calibration, a 5 × 7 ChArUco Board was placed on the table as a calibration object. The robotic arm moved the end-effector to twenty different poses ($H_{E_i}^G$, end-effector poses in the global coordinate frame *G*) and the in-hand camera captured images of the calibration object at each pose. The corners of the ChArUco Board were detected in each image and used to estimate the pose of the board ($H_B^{C_i}$) in the camera coordinate frame *C* using OpenCV libraries [67]. Then, the hand–eye transformation matrix H_C^E was calculated using a previously reported method [68], which involves solving the following:

$$A_i X = X B_i \quad \text{for } i = 1, 2, \ldots, 20 \tag{21}$$

where $A_i = H_{C_i}^{C_{i+1}} = H_B^{C_{i+1}} (H_B^{C_i})^{-1}$ is the transformation matrix between two camera poses, $B_i = H_{E_i}^{E_{i+1}} = (H_{E_{i+1}}^G)^{-1} H_{E_i}^G$ is the transformation matrix between two end-effector poses, and $X = H_C^E$ is the unknown hand–eye transformation matrix. The method minimizes the error in these equations to accurately estimate $X = H_C^E$.

With the online calibration results, any point captured by the RGB-D camera $P_C = [x_C, y_C, z_C]^T$ can be expressed in the global coordinate frame $P_G = [x_G, y_G, z_G]^T$ by homogeneous transformation

$$\begin{bmatrix} P_G \\ 1 \end{bmatrix} = H_E^G H_C^E \begin{bmatrix} P_C \\ 1 \end{bmatrix} \tag{22}$$

where H_C^E is the calibrated hand–eye transformation matrix and H_E^G represents the transformation matrix of the UR5 end-effector pose with respect to the global coordinate frame G, which can be obtained using the forward kinematics of the UR5 robotic arm.

For the vision-guided grasping, multiple unknown objects were placed on the table in various unknown positions and orientations, as shown in Fig. 15(c). One cylinder was tilted at a specific angle by connecting it to a cable. All objects were positioned separately to avoid contacting each other. To start the experiment, the robotic arm moved the soft hand to five designated positions (top, top-left, top-right, top-forward, top-back), which ensured the in-hand RGB-D camera comprehensively scanned all object surfaces, as illustrated in Fig. 15(b). During the scanning, the in-hand RGB-D camera captured sequences of RGB images and depth images, which were processed to construct a raw point cloud of each object using a contour detection algorithm from the OpenCV library [67] and transformed into the global coordinate frame using (22) for subsequent point cloud merging.

The point clouds captured from different views were merged using an initial alignment via random sampling consensus (RANSAC) [69], followed by fine registration through the iterative closest point (ICP) algorithm [70], [71], which minimizes pointwise Euclidean distances between corresponding points by finding the optimal rotational matrix $\mathbf{R}$ and translation vector $\mathbf{T}$

$$\underset{\mathbf{T}\in\mathbb{R}^3,\ \mathbf{R}\in SO(3)}{\text{minimize}} \sum_{i=1}^{N} \| \mathbf{R}x_{\text{new}}^{(i)} + \mathbf{T} - x_{\text{acc}}^{(i)} \|_2^2 \tag{23}$$

where $x_{\text{new}}^{(i)}$ and $x_{\text{acc}}^{(i)}$ represent the ith point in the newly captured point cloud and the accumulated point cloud, respectively, and N is the number of points in the cloud. After merging, the combined point cloud was downsampled to reduce computational cost. The combined point cloud of all the objects is shown in Fig. 15(d).

To segment individual objects from the combined point cloud, the density-based spatial clustering of applications with noise (DBSCAN) algorithm [72] was applied, with iterative adjustment of its hyperparameters ($eps = 0.025$ and $MinPts = 225$) to provide accurate and stable clustering results. Once the individual point clouds for each object were obtained, an approximate MVBB [73], [74] was generated for each object [see Fig. 15(d)] and the center point, dimension, and orientation of each MVBB were obtained. The orientation of the MVBB is indicated by the coordinate frame in Fig. 15(d), where the x-axis is aligned with the main axis (along the longest edge) and the y-axis is along the shortest edge. The information from MVBB formed the basis for designing a grasping strategy for the soft hand.

The grasping orientation for each object was determined based on the MVBB orientation. Specifically, the x-, y-, and z-axes of the soft hand coordinate frame [aligned with the camera coordinate frame in Fig. 15(a)] should be in the same direction as the x-, y-, and z-axes of the MVBB so that the soft hand can always grasp the shortest edge of objects. Subsequently, the grasping mode (pinch grasp or power grasp) was determined based on the approaching direction for each object [z-axis in Fig. 15(d)]. An approaching direction toward the table, as seen with the red jello box and tennis ball, necessitated a pinch grasp to avoid contact between the fingers and the table surface, while for the other approaching direction, a power grasp was used for enhanced stability during grasping.

To determine the motor input required for grasping each object, a discretized control scheme was developed, which correlates the object MVBB dimensions with predefined motor inputs. For both power and pinch grasps, the grasping dimensional limits (obtained in Section III-C) were discretized evenly into five ranges: [25 mm, 38.4 mm), [38.4 mm, 51.8 mm), [51.8 mm, 65.2 mm), [65.2 mm, 78.6 mm), [78.6 mm, 92 mm] for power grasp and [15 mm, 30.4 mm), [30.4 mm, 45.8 mm), [45.8 mm, 61.2 mm), [61.2 mm, 76.6 mm), [76.6 mm, 92 mm] for pinch grasp. Each range for both grasp modes was associated with a motor input that has been tested for the soft hand to be able to securely grasp objects within that dimension range. For each object, the dimension of the MVBB shortest edge was classified into a certain range, and the corresponding motor input was selected accordingly. For example, the red chip depicted in Fig. 15(c) has its shortest MVBB edge computed as 75.6 mm, falling within the range [65.2 mm, 78.6 mm) for a power grasp, which will automatically register the soft hand to the corresponding motor input. This method of determining motor input proves to be effective due to the inherent compliance and softness of the soft hand, allowing it to adapt to various object shapes and sizes.

With the obtained grasp pose and the motor input, the UR5 robotic arm could guide the soft hand to approach each object from the specified grasp direction and grasp the object by employing the determined motor input. Consequently, all the objects were sequentially collected in a basket, as shown in Fig. 15(e). A video demonstrating the vision-guided grasping can be found in the supplemental Movie S6.

D. Vision-Based Slip Detection and Compensation

Human hands can adaptively respond to external disturbances to maintain a stable grasp by quickly adjusting their grip strength. However, for soft robotic hands, it remains a challenge to adapt to external disturbances (e.g., dragging forces or the shifting weight of a container during filling) due to the difficulty in detecting slip events without sufficient sensory feedback. The integration of the in-hand camera in our soft hand could address this limitation by enabling efficient slip detection and compensation based on visual feedback.

To evaluate this capability, we conducted an experiment in which the soft hand grasped a plastic bottle with fingertips while water was gradually filled into it to impose an increasing external load, as shown in Fig. 16 and the supplemental Movie S7. Initially, an appropriate grasping force was applied to securely hold the empty bottle. An ArUco marker [75] was attached to the bottle surface, and its position was continuously tracked by the in-hand camera. A slip condition was determined when the marker displacement along the gravitational axis exceeded a predefined threshold $THRES$

$$|x_t - x_{t-\Delta t}| > THRES \tag{24}$$

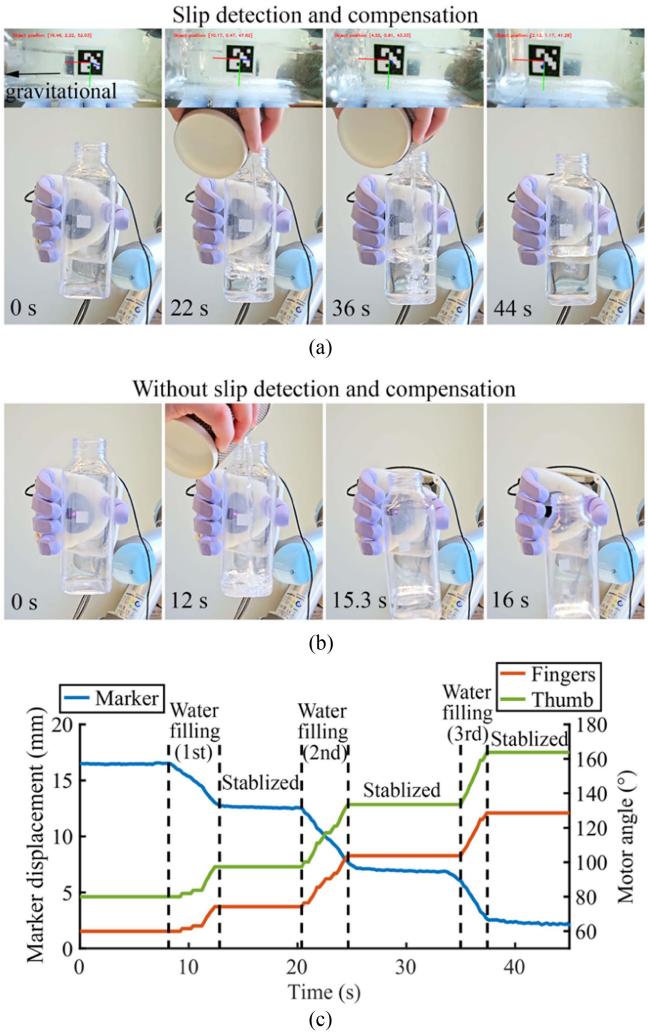

Fig. 16. Vision-based slip detection and compensation during a water filling task. (a) Bottle was stably grasped with visual feedback from the in-hand camera. The in-hand camera view is shown above, with the ArUco marker detected. (b) Without slip detection and compensation, the bottle slipped as water was added. (c) Time series of the ArUco marker displacement along the gravitational direction and the corresponding motor angles of the thumb and other fingers, recorded during the slip detection and compensation process.

where x_t denotes the marker position along the gravitational axis at time t, and Δt is the sampling interval. In this experiment, the threshold and interval were set to $THRES = 0.18$ mm and $\Delta t = 0.2$ s, respectively. When a slip event was detected, the slip compensation controller adaptively increased the motor angles of the fingers to strengthen the grasp. The increase of the motor angle was proportional to the magnitude of marker displacement

$$\Delta\theta = k_s \cdot |x_t - x_{t-\Delta t}| \tag{25}$$

where k_s is a proportional gain tuned empirically to ensure efficient compensation. In this experiment, $k_s = 7.75$ was used for the thumb and $k_s = 9.46$ for the other four fingers. This allows for adaptive compensation in real time, depending on the amount of slip.

As shown in Fig. 16(a), with the slip detection and compensation controller, the soft hand successfully maintained a stable grasp on the bottle while approximately 200 mL of water (∼200 g) was added, which is about five times the initial bottle weight (∼40 g). The water was added in three stages, and the soft hand can restabilize the grasp after each water addition. In contrast, without the vision-based slip compensation strategy, the bottle began to slip when the water was added at the first stage (∼65 mL) and subsequently fell from the hand, as shown in 16(b). The corresponding time-series data of marker displacement along the gravitational direction and the corresponding motor angles of the thumb and other fingers are shown in Fig. 16(c). A video comparing the grasp stability with and without vision-based slip detection and compensation during a water filling task is provided in the supplemental Movie S7. These results demonstrate that integrating an in-hand camera enables effective slip detection and adaptive real-time grasp compensation. This capability significantly enhances the grasp stability and environmental adaptability of the soft robotic hand in dynamic and unstructured environments.

E. Visually Servoed In-Hand Manipulation

A hierarchical, visually servoed controller was developed to enable in-hand object manipulation using visual feedback from the in-palm RGB-D camera. This controller allows the soft hand to autonomously adjust the pose of a grasped object to match target poses. The controller is structured into three hierarchical layers: the vision layer, the tactical layer, and the execution layer. In the vision layer, the in-hand RGB-D camera continuously tracks the 6-D pose of the object by detecting the ArUco marker [75] attached to its surface. The object pose is then compared to a target pose to compute the pose error. In the tactical layer, this pose error is interpreted and mapped to a set of corresponding finger movement primitives (e.g., F/E and AD/AB movements of the thumb and opposing fingers). Finally, in the execution layer, the fingers are actuated using the PID control to realize the selected primitives so that the soft hand can gradually adjust the pose of the object in real time. This hierarchical structure enables task-driven motion planning and then assigns distinct roles to each finger to demonstrate motor coordination in the high-dimensional actuator space of the soft hand.

To evaluate the controller, we implemented three representative visually servoed in-hand object manipulation tasks: in-plane rotation around the z-axis, translation along the x-axis, and translation along the z-axis, as shown in Fig. 17. These tasks were selected from the six basic in-hand manipulation types (see Fig. 14). Three tasks were chosen because they have minimal coupling with motions in other directions, and are thus effective to demonstrate the capabilities of the proposed controller. For these tasks, a 3-D-printed box was used, which has a dimension of 60 mm × 90 mm × 60 mm. During the initial pinch grasp of this box, the average normalized manipulability value w_{norm} of all fingers was calculated as 0.71, which is greater than 0.5 (high manipulability region as discussed in Section III-D), ensuring a high manipulation capability for the soft hand.

As shown in Fig. 17(a), the soft hand initially grasped the box, and then performed in-plane rotation along the z-axis to -10°

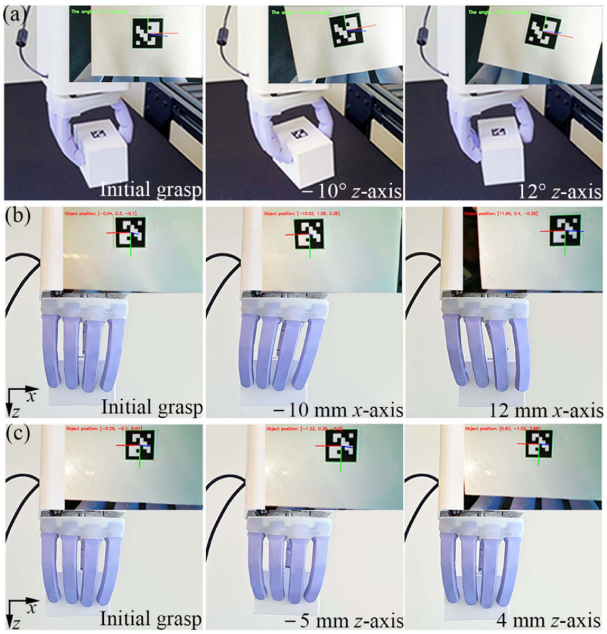

Fig. 17. Visually servoed in-hand manipulation of a 3-D-printed box using a hierarchical controller. (a) In-plane rotation around the z-axis to $-10°$ and $12°$. (b) Translation along the x-axis by -10 mm and 12 mm. (c) Translation along the z-axis with displacements of -5 mm and 4 mm.

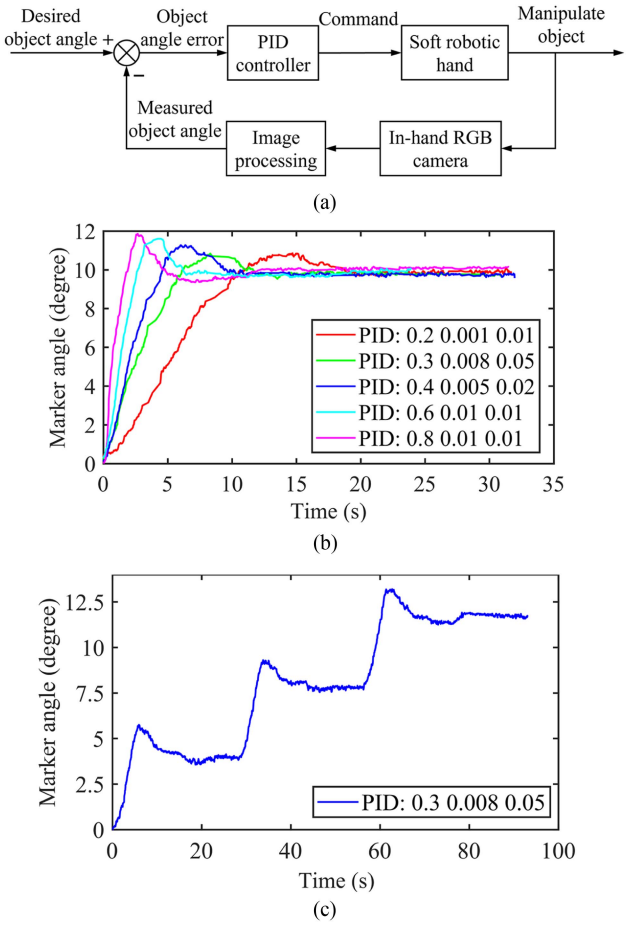

Fig. 18. Visual servo PID controller in the execution layer. (a) Schematic of the PID controller. (b) Tuning of parameters (K_P, K_I, and K_D) and the corresponding response of object angle during the z-axis in-hand rotation. (c) Step response of the PID controller.

and $12°$ using opposite AD/AB movements of the thumb and opposing fingers. The coupled rotation around the x- and y-axes during manipulation was measured to be less than $2°$. A video of the z-axis in-hand rotation is provided in the supplemental Movie S8. In Fig. 17(b), the box was translated by -10 mm and 12 mm along the x-axis from its initial position, which is achieved through lateral AD/AB movements in the same direction across all fingers. In Fig. 17(c), translation along the z-axis (toward and away from the palm) is demonstrated with target displacements of -5 mm and 4 mm, realized through synchronized F/E movements of the fingers. In all the in-hand manipulation tasks, the hierarchical controller decomposed the visual pose error into coordinated finger motion primitives, which were then executed via PID control using continuous visual feedback to adjust the object pose precisely.

The visual servo PID controller within the execution layer was used to regulate motor positions during the manipulation tasks, as illustrated in Fig. 18(a). The PID parameters (K_P, K_I, and K_D) were tuned experimentally to achieve stable and responsive control. Fig. 18(b) shows the stepwise responses of the PID controlled with different values of K_P, K_I, and K_D during the in-plane rotation around the z-axis. The optimal parameters were determined to be $K_P = 0.3, K_I = 0.008$, and $K_D = 0.05$, achieving a rise time of 6.7 s and a steady-state error of 3.4% . With the chosen PID parameters, we also showed the tracking of stepwise increases of the measured object angle around the z-axis, as shown in Fig. 18(c).

V. Conclusion

In this article, a cable-driven soft robotic hand inspired by the human hand was proposed, which consisted of a palm base with an in-hand RGB-D camera and five soft fingers (each of which was actuated by two motors through cables and thus can perform F/E and AD/AB movements independently). Mathematical models were established for the soft hand to analyze its kinematics, statics, and manipulability, and characterization was performed to analyze the performance of the fingers and hand. Experiments demonstrated that the soft hand was capable of achieving grasping of delicate objects and dexterous grasping of multiple objects in hand, as well as performing various dexterous in-hand manipulation tasks. Despite these capabilities, the current design still has limitations; for example, the hand cannot grasp objects with very small diameters from the table surface. Future work will address this challenge by integrating adaptive fingertips or introducing mechanical refinements to the soft fingers.

A key feature of the proposed hand was the integration of an in-hand RGB-D camera, which enabled vision-guided grasp, vision-based slip detection and compensation, as well as visually servoed in-hand manipulation. Compared to vision-based tactile or multimodal sensors [76], [77], [78], the in-hand RGB-D camera does not require direct physical contact with objects and can provide rich pose and depth information of target objects

during the pregrasp planning stage. Furthermore, during grasp and manipulation, the in-hand RGB-D camera can continuously provide global pose information of the grasped object and thus enable slip detection with real-time grasp adjustment and closed-loop visually servoed in-hand manipulation. Overall, the soft hand exhibits a high level of dexterity and intelligence, making it suitable for diverse applications, including fruit picking and sorting, household object grasping and manipulation, and potential use in prosthetic hands and as an auxiliary hand for humans. Using the visual feedback from the in-hand camera, human–robot interactive grasping experiments of the soft hand could also be realized through deep learning methods, which will be explored in the future.

REFERENCES

[1] R. Balasubramanian and V. J. Santos, *The Human Hand as an Inspiration for Robot Hand Development*. Cham, Switzerland: Springer, 2014.

[2] Y. Wang, T. Hao, Y. Liu, H. Xiao, S. Liu, and H. Zhu, "Anthropomorphic soft hand: Dexterity, sensing, and machine learning," *Actuators*, vol. 13, no. 3, 2024, Art. no. 84.

[3] T. Inoue and S. Hirai, *Mechanics and Control of Soft-Fingered Manipulation*. London, U.K.: Springer, 2009.

[4] M. Laffranchi et al., "The Hannes hand prosthesis replicates the key biological properties of the human hand," *Sci. Robot.*, vol. 5, no. 46, 2020, Art. no. eabb0467.

[5] B.-Y. Sun et al., "Design principle of a dual-actuated robotic hand with anthropomorphic self-adaptive grasping and dexterous manipulation abilities," *IEEE Trans. Robot.*, vol. 38, no. 4, pp. 2322–2340, Aug. 2022.

[6] K. Gilday, C. Sirithunge, F. Iida, and J. Hughes, "Embodied manipulation with past and future morphologies through an open parametric hand design," *Sci. Robot.*, vol. 10, no. 102, 2025, Art. no. eads6437.

[7] "Shadow robot company," Dexterous hand series. [Online]. Available: https://www.shadowrobot.com/dexterous-hand-series/

[8] M. Grebenstein et al., "The DLR hand arm system," in *Proc. IEEE Int. Conf. Robot. Autom.*, 2011, pp. 3175–3182.

[9] D.-H. Lee, J.-H. Park, S.-W. Park, M.-H. Baeg, and J.-H. Bae, "Kitech-hand: A highly dexterous and modularized robotic hand," *IEEE/ASME Trans. Mechatron.*, vol. 22, no. 2, pp. 876–887, Apr. 2017.

[10] K. Shaw, A. Agarwal, and D. Pathak, "Leap hand: Low-cost, efficient, and anthropomorphic hand for robot learning," in *Proc. Robot.: Sci. Syst.*, Daegu, Republic of Korea, Jul. 2023.

[11] A. Zorin et al., "RUKA: Rethinking the design of humanoid hands with learning," in *Proc. Robot.: Sci. Syst.*, Los Angeles, CA, USA, Jun. 2025.

[12] C. C. Christoph et al., "ORCA: An open-source, reliable, cost-effective, anthropomorphic robotic hand for uninterrupted dexterous task learning," 2025, *arXiv:2504.04259*.

[13] A.-V. Ho and S. Hirai, *Mechanics of Localized Slippage in Tactile Sensing: And Application to Soft Sensing Systems*. Cham, Switzerland: Springer, 2014.

[14] J. Shintake, V. Cacucciolo, D. Floreano, and H. Shea, "Soft robotic grippers," *Adv. Mater.*, vol. 30, no. 29, 2018, Art. no. 1707035.

[15] A. Billard and D. Kragic, "Trends and challenges in robot manipulation," *Science*, vol. 364, no. 6446, 2019, Art. no. eaat8414.

[16] Z. Zhou et al., "A sensory soft robotic gripper capable of learning-based object recognition and force-controlled grasping," *IEEE Trans. Autom. Sci. Eng.*, vol. 21, no. 1, pp. 844–854, Jan. 2022.

[17] H. Zhao, K. O'brien, S. Li, and R. F. Shepherd, "Optoelectronically innervated soft prosthetic hand via stretchable optical waveguides," *Sci. Robot.*, vol. 1, no. 1, 2016, Art. no. eaai7529.

[18] L. Zhou, L. Ren, Y. Chen, S. Niu, Z. Han, and L. Ren, "Bio-inspired soft grippers based on impactive gripping," *Adv. Sci.*, vol. 8, no. 9, 2021, Art. no. 2002017.

[19] G. Gu, N. Zhang, C. Chen, H. Xu, and X. Zhu, "Soft robotics enables neuroprosthetic hand design," *ACS Nano*, vol. 17, no. 11, pp. 9661–9672, 2023.

[20] G. Gu et al., "A soft neuroprosthetic hand providing simultaneous myoelectric control and tactile feedback," *Nat. Biomed. Eng.*, vol. 7, no. 4, pp. 589–598, 2023.

[21] J. Zhou et al., "A soft-robotic approach to anthropomorphic robotic hand dexterity," *IEEE Access*, vol. 7, pp. 101483–101495, 2019.

[22] Y. Cui, X.-J. Liu, X. Dong, J. Zhou, and H. Zhao, "Enhancing the universality of a pneumatic gripper via continuously adjustable initial grasp postures," *IEEE Trans. Robot.*, vol. 37, no. 5, pp. 1604–1618, Oct. 2021.

[23] S. Puhlmann, J. Harris, and O. Brock, "Rbo hand 3: A platform for soft dexterous manipulation," *IEEE Trans. Robot.*, vol. 38, no. 6, pp. 3434–3449, Dec. 2022.

[24] A. M. Dollar and R. D. Howe, "The highly adaptive SDM hand: Design and performance evaluation," *Int. J. Robot. Res.*, vol. 29, no. 5, pp. 585–597, 2010.

[25] M. Manti, T. Hassan, G. Passetti, N. D'Elia, C. Laschi, and M. Cianchetti, "A bioinspired soft robotic gripper for adaptable and effective grasping," *Soft Robot.*, vol. 2, no. 3, pp. 107–116, 2015.

[26] G. Salvietti, Z. Iqbal, I. Hussain, D. Prattichizzo, and M. Malvezzi, "The co-gripper: A wireless cooperative gripper for safe human robot interaction," in *Proc. IEEE/RSJ Int. Conf. Intell. Robots Syst.*, 2018, pp. 4576–4581.

[27] H. Zhou, C. Tawk, and G. Alici, "A 3D printed soft robotic hand with embedded soft sensors for direct transition between hand gestures and improved grasping quality and diversity," *IEEE Trans. Neural Syst. Rehabil. Eng.*, vol. 30, pp. 550–558, 2022.

[28] M. Tavakoli, R. Batista, and L. Sgrigna, "The UC softhand: Light weight adaptive bionic hand with a compact twisted string actuation system," *Actuators*, vol. 5, no. 1, 2016.

[29] M. G. Catalano, G. Grioli, E. Farnioli, A. Serio, C. Piazza, and A. Bicchi, "Adaptive synergies for the design and control of the pisa/iit softhand," *Int. J. Robot. Res.*, vol. 33, no. 5, pp. 768–782, 2014.

[30] C. Della Santina, C. Piazza, G. Grioli, M. G. Catalano, and A. Bicchi, "Toward dexterous manipulation with augmented adaptive synergies: The pisa/iit softhand 2," *IEEE Trans. Robot.*, vol. 34, no. 5, pp. 1141–1156, Oct. 2018.

[31] A. Mohammadi et al., "A practical 3D-printed soft robotic prosthetic hand with multi-articulating capabilities," *PLoS One*, vol. 15, no. 5, 2020, Art. no. e0232766.

[32] P. Weiner, J. Starke, S. Rader, F. Hundhausen, and T. Asfour, "Designing prosthetic hands with embodied intelligence: The kit prosthetic hands," *Front. Neurorobot.*, vol. 16, 2022, Art. no. 815716.

[33] G. P. Kontoudis, M. Liarokapis, and K. G. Vamvoudakis, "An adaptive, humanlike robot hand with selective interdigitation: Towards robust grasping and dexterous, in-hand manipulation," in *Proc. IEEE-RAS Int. Conf. Humanoid Robots*, 2019, pp. 251–258.

[34] G. P. Kontoudis, M. Liarokapis, K. G. Vamvoudakis, and T. Furukawa, "An adaptive actuation mechanism for anthropomorphic robot hands," *Front. Robot. AI*, vol. 6, 2019, Art. no. 47.

[35] Y. Yan, Y. Wang, X. Chen, C. Shi, J. Yu, and C. Cheng, "A tendon-driven prosthetic hand using continuum structure," in *Proc. IEEE Eng. Med. Biol. Soc.*, 2020, pp. 4951–4954.

[36] Y. Yan, X. Chen, C. Cheng, and Y. Wang, "Design, kinematic modeling and evaluation of a novel soft prosthetic hand with abduction joints," *Med. Novel Technol. Devices*, vol. 15, 2022, Art. no. 100151.

[37] L. U. Odhner et al., "A compliant, underactuated hand for robust manipulation," *Int. J. Robot. Res.*, vol. 33, no. 5, pp. 736–752, 2014.

[38] L. U. Odhner and A. M. Dollar, "Stable, open-loop precision manipulation with underactuated hands," *Int. J. Robot. Res.*, vol. 34, no. 11, pp. 1347–1360, 2015.

[39] R. Ma and A. Dollar, "Yale openhand project: Optimizing open-source hand designs for ease of fabrication and adoption," *IEEE Robot. Autom. Mag.*, vol. 24, no. 1, pp. 32–40, Mar. 2017.

[40] M. Liarokapis and A. M. Dollar, "Combining analytical modeling and learning to simplify dexterous manipulation with adaptive robot hands," *IEEE Trans. Autom. Sci. Eng.*, vol. 16, no. 3, pp. 1361–1372, Jul. 2019.

[41] R. R. Ma and A. M. Dollar, "An underactuated hand for efficient finger-gaiting-based dexterous manipulation," in *Proc. IEEE Int. Conf. Robot. Biomimetics*, 2014, pp. 2214–2219.

[42] A. S. Morgan, K. Hang, B. Wen, K. Bekris, and A. M. Dollar, "Complex in-hand manipulation via compliance-enabled finger gaiting and multimodal planning," *IEEE Robot. Autom. Lett.*, vol. 7, no. 2, pp. 4821–4828, Apr. 2022.

[43] S. Hutchinson, G. D. Hager, and P. I. Corke, "A tutorial on visual servo control," *IEEE Trans. Robot. Autom.*, vol. 12, no. 5, pp. 651–670, Oct. 1996.

[44] G. Flandin, F. Chaumette, and E. Marchand, "Eye-in-hand/eye-to-hand cooperation for visual servoing," in *Proc. Int. Conf. Robot. Autom.*, 2000, vol. 3, pp. 2741–2746.

[45] C. Choi, W. Schwarting, J. DelPreto, and D. Rus, "Learning object grasping for soft robot hands," *IEEE Robot. Autom. Lett.*, vol. 3, no. 3, pp. 2370–2377, Jul. 2018.

[46] K. Hang, W. G. Bircher, A. S. Morgan, and A. M. Dollar, "Hand–object configuration estimation using particle filters for dexterous in-hand manipulation," *Int. J. Robot. Res.*, vol. 39, no. 14, pp. 1760–1774, 2020.

[47] B. Wen, C. Mitash, B. Ren, and K. E. Bekris, "se (3)-tracknet: Data-driven 6D pose tracking by calibrating image residuals in synthetic domains," in *Proc. IEEE/RSJ Int. Conf. Intell. Robots Syst.*, 2020, pp. 10367–10373.

[48] A. S. Morgan, B. Wen, J. Liang, A. Boularias, A. M. Dollar, and K. Bekris, "Vision-driven compliant manipulation for reliable; high-precision assembly tasks," in *Proc. Robot.: Sci. Syst.*, Jul. 2021.

[49] H. Li, J. Tan, and H. He, "Magichand: Context-aware dexterous grasping using an anthropomorphic robotic hand," in *Proc. IEEE Int. Conf. Robot. Autom.*, 2020, pp. 9895–9901.

[50] K. Hang, W. G. Bircher, A. S. Morgan, and A. M. Dollar, "Manipulation for self-identification, and self-identification for better manipulation," *Sci. Robot.*, vol. 6, no. 54, 2021, Art. no. eabe1321.

[51] T. Ozsoy, Z. Oner, and S. Oner, "An attempt to gender determine with phalanx length and the ratio of phalanxes to whole phalanx length in direct hand radiography," *Med.*, vol. 8, no. 3, pp. 692–7, 2019.

[52] R. R. Ma, J. T. Belter, and A. M. Dollar, "Hybrid deposition manufacturing: Design strategies for multimaterial mechanisms via three-dimensional printing and material deposition," *J. Mech. Robot.*, vol. 7, no. 2, 2015, Art. no. 021002.

[53] R. R. Ma and A. M. Dollar, "Linkage-based analysis and optimization of an underactuated planar manipulator for in-hand manipulation," *J. Mech. Robot.*, vol. 6, no. 1, 2014, Art. no. 011002.

[54] H. Dong, E. Asadi, C. Qiu, J. Dai, and I.-M. Chen, "Grasp analysis and optimal design of robotic fingertip for two tendon-driven fingers," *Mech. Mach. Theory*, vol. 130, pp. 447–462, 2018.

[55] P. Capsi-Morales, G. Grioli, C. Piazza, A. Bicchi, and M. G. Catalano, "Exploring the role of palm concavity and adaptability in soft synergistic robotic hands," *IEEE Robot. Autom. Lett.*, vol. 5, no. 3, pp. 4703–4710, Jul. 2020.

[56] M. A. Roa et al., "Towards a functional evaluation of manipulation performance in dexterous robotic hand design," in *Proc. IEEE Int. Conf. Robot. Autom.*, 2014, pp. 6800–6807.

[57] H. Kawasaki, T. Furukawa, S. Ueki, and T. Mouri, "Virtual robot teaching based on motion analysis and hand manipulability for multi-fingered robot," *J. Adv. Mech. Des. Syst. Manuf.*, vol. 3, no. 1, pp. 1–12, 2009.

[58] T. Yoshikawa, "Manipulability of robotic mechanisms," *Int. J. Robot. Res.*, vol. 4, no. 2, pp. 3–9, 1985.

[59] T. Feix, J. Romero, H.-B. Schmiedmayer, A. M. Dollar, and D. Kragic, "The grasp taxonomy of human grasp types," *IEEE Trans. Hum.-Mach. Syst.*, vol. 46, no. 1, pp. 66–77, Feb. 2016.

[60] B. Calli, A. Singh, A. Walsman, S. Srinivasa, P. Abbeel, and A. M. Dollar, "The YCB object and model set: Towards common benchmarks for manipulation research," in *Proc. IEEE Int. Conf. Robot. Autom.*, 2015, pp. 510–517.

[61] C. Gabellieri et al., "Grasp it like a pro: Grasp of unknown objects with robotic hands based on skilled human expertise," *IEEE Robot. Autom. Lett.*, vol. 5, no. 2, pp. 2808–2815, Apr. 2020.

[62] K. Huebner, S. Ruthotto, and D. Kragic, "Minimum volume bounding box decomposition for shape approximation in robot grasping," in *Proc. IEEE Int. Conf. Robot. Autom.*, 2008, pp. 1628–1633.

[63] E. G. Ribeiro, R. de Queiroz Mendes, and V. Jr Grassi, "Real-time deep learning approach to visual servo control and grasp detection for autonomous robotic manipulation," *Robot. Auton. Syst.*, vol. 139, 2021, Art. no. 103757.

[64] J. Mahler et al., "Dex-Net 2.0: Deep learning to plan robust grasps with synthetic point clouds and analytic grasp metrics," in *Proc. Robot.: Sci. Syst.*, Cambridge, MA, USA, Jul. 2017.

[65] O. M. Andrychowicz et al., "Learning dexterous in-hand manipulation," *Int. J. Robot. Res.*, vol. 39, no. 1, pp. 3–20, 2020.

[66] F. Ficuciello, A. Migliozzi, G. Laudante, P. Falco, and B. Siciliano, "Vision-based grasp learning of an anthropomorphic hand-arm system in a synergy-based control framework," *Sci. Robot.*, vol. 4, no. 26, 2019, Art. no. eaao4900.

[67] G. Bradski, "The openCV library," *Dobb's J. Softw. Tools*, vol. 25, no. 11, pp. 120–123, 2000.

[68] R. Horaud and F. Dornaika, "Hand-eye calibration," *Int. J. Robot. Res.*, vol. 14, no. 3, pp. 195–210, 1995.

[69] C.-Y. Tsai, C.-W. Wang, and W.-Y. Wang, "Design and implementation of a ransac RGB-D mapping algorithm for multi-view point cloud registration," in *Proc. CACS Int. Autom. Control Conf.*, 2013, pp. 367–370.

[70] D. Holz, A. E. Ichim, F. Tombari, R. B. Rusu, and S. Behnke, "Registration with the point cloud library: A modular framework for aligning in 3-D," *IEEE Robot. Autom. Mag.*, vol. 22, no. 4, pp. 110–124, Dec. 2015.

[71] F. A. Maken, F. Ramos, and L. Ott, "Speeding up iterative closest point using stochastic gradient descent," in *Proc. IEEE Int. Conf. Robot. Autom.*, 2019, pp. 6395–6401.

[72] M. Ester, H.-P. Kriegel, J. Sander, and X. Xu, "A density-based algorithm for discovering clusters in large spatial databases with noise," in *Proc. Int. Conf. Knowl. Discov. Data Mining*, 1996, vol. 96, no. 34, pp. 226–231.

[73] G. Barequet and S. Har-Peled, "Efficiently approximating the minimum-volume bounding box of a point set in three dimensions," *J. Algorithms*, vol. 38, no. 1, pp. 91–109, 2001.

[74] C.-T. Chang, B. Gorissen, and S. Melchior, "Fast oriented bounding box optimization on the rotation group so (3, $\mathbb{R}$)," *ACM Trans. Graph.*, vol. 30, no. 5, pp. 1–16, 2011.

[75] R. Munoz-Salinas, "Aruco: A minimal library for augmented reality applications based on opencv," Universidad de Córdoba, Córdoba, Spain, 2012.

[76] W. Yuan, S. Dong, and E. H. Adelson, "Gelsight: High-resolution robot tactile sensors for estimating geometry and force," *Sensors*, vol. 17, no. 12, 2017, Art. no. 2762.

[77] S. Zhang, Y. Yang, J. Shan, F. Sun, H. Xue, and B. Fang, "Palmtac: A vision-based tactile sensor leveraging distributed-modality design and modal-matching recognition for soft hand perception," *IEEE J. Sel. Top. Signal Process.*, vol. 18, no. 3, pp. 288–298, Apr. 2024.

[78] S. Q. Liu and E. H. Adelson, "A passively bendable, compliant tactile palm with robotic modular endoskeleton optical (romeo) fingers," in *Proc. IEEE Int. Conf. Robot. Autom.*, 2024, pp. 691–697.

Zhanfeng Zhou (Member, IEEE) received the B.Eng. and M.Eng. degrees in mechatronics engineering from the Harbin Institute of Technology, Harbin, China, in 2018 and 2020, respectively. He is currently working toward the Ph.D. degree in mechanical engineering with the University of Toronto, Toronto, Canada.

His research interests include soft robotics, dexterous robotic hands, wearable electronics, prosthetics, rehabilitation robots, and assistive robots.

Runze Zuo (Student Member, IEEE) received the B.A.Sc. degree in computer engineering from the University of Toronto, Toronto, Canada, in 2023. He is currently working toward the Ph.D. degree in mechanical engineering with the University of Michigan, Ann Arbor, MI, USA.

His research interests include the design and control of performance soft robotic systems for real-world deployment.

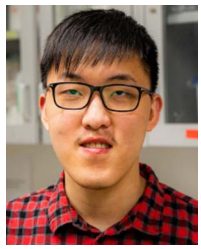

Matthew Du is currently working toward the B.A.Sc. degree in mechanical engineeringat the University of Toronto in Toronto, Canada and he expects to compete the degree in 2026.

He was an undergraduate Research Assistant with the Microfluidics and BioMEMS Lab, University of Toronto, in 2022. He also held positions as an Aircraft Performance Intern with Bombardier, Toronto, from 2024 to 2025. His research interests include computational fluid dynamics, computer vision, soft robotics, machine learning, and engineering for accessibility.

Shaojia Wang received the B.A.Sc. degree in 2023 from the University of Toronto, Toronto, Canada, where he is currently working toward the Ph.D. degree, both in mechanical engineering.

His research interests include machine learning assisted multimaterial 3-D printing and soft robotics.

Sebastian Levy (Member, IEEE) received the B.A.Sc. degree in mechanical engineering from the University of Toronto, Toronto, Canada, in 2023, and the M.S. degree in mechanical engineering and engineering and technology innovation management from Carnegie Mellon University, Pittsburgh, PA, USA, in 2025.

He is currently a System Product Design Engineer with Apple, Cupertino, CA, USA. His research interests include wearable health sensing, computer vision, soft robotics, and biomechanics.

Yu Sun (Fellow, IEEE) received the B.S. degree in electrical engineering from the Dalian University of Technology, Dalian, China, in 1996, the M.S. degree from the Institute of Automation, Chinese Academy of Sciences, Beijing, China, in 1999, and the second M.S. degree in electrical engineering and the Ph.D. degree in mechanical engineering from the University of Minnesota, Minneapolis, MN, USA, in 2001 and 2003, respectively.

He is currently a Professor with the University of Toronto, Toronto, Canada.

Dr. Sun was an elected Fellow of the American Society of Mechanical Engineers, the American Association for the Advancement of Science, the National Academy of Inventors, the Canadian Academy of Engineering, and the Royal Society of Canada for his work on micro–nano devices and robotic systems.

Xinyu Liu (Member, IEEE) received the B.Eng. and M.Eng. degrees from the Harbin Institute of Technology, Harbin, China, in 2002 and 2004, respectively, and the Ph.D. degree from the University of Toronto, Toronto, Canada, in 2009, all in mechanical engineering.

He then completed an NSERC Postdoctoral Fellowship with the Department of Chemistry and Chemical Biology, Harvard University, Cambridge, MA, USA, from 2009 to 2011. He is currently a Professor with the Department of Mechanical and Industrial Engineering, University of Toronto. His research interests include micro/nano robotics, soft robotics, and flexible/stretchable sensors and electronics.

Prof. Liu is a Fellow of the Canadian Academy of Engineering, the Engineering Institute of Canada, the American Society of Mechanical Engineers, and the Canadian Society for Mechanical Engineering, and an Elected Member of the European Academy of Sciences and Arts.